

Paleoceanography and Paleoclimatology

RESEARCH ARTICLE

10.1029/2020PA003936

Key Points:

- Precipitation over northern northeastern Brazil decreased from the mid- to the late Holocene
- The meridional migration range of the Intertropical Convergence Zone contracted from the mid- to the late Holocene
- Together with the intensification of the regional Walker circulation, our results reconcile previously conflicting records

Supporting Information:

Supporting Information may be found in the online version of this article.

Correspondence to:

C. M. Chiessi,
chiessi@usp.br










Citation:

Chiessi, C. M., Mulitza, S., Taniguchi, N. K., Prange, M., Campos, M. C., Häggi, C., et al. (2021). Mid- to late-Holocene contraction of the Intertropical Convergence Zone over northeastern South America. *Paleoceanography and Paleoclimatology*, 36, e2020PA003936. <https://doi.org/10.1029/2020PA003936>

Received 28 MAR 2020

Accepted 24 MAR 2021

Mid- to Late Holocene Contraction of the Intertropical Convergence Zone Over Northeastern South America

C. M. Chiessi¹ , S. Mulitza² , N. K. Taniguchi³, M. Prange² , M. C. Campos¹ , C. Häggi^{2,4} , E. Schefuß², T. M. L. Pinho⁵ , T. Frederichs^{2,6} , R. C. Portillo-Ramos², S. H. M. Sousa³, S. Crivellari⁵ , and F. W. Cruz⁵ 

¹School of Arts, Sciences and Humanities, University of São Paulo, São Paulo, Brazil, ²MARUM - Center for Marine Environmental Sciences, University of Bremen, Bremen, Germany, ³Institute of Oceanography, University of São Paulo, São Paulo, Brazil, ⁴Department of Earth Sciences, University of Southern California, Los Angeles, CA, USA, ⁵Institute of Geosciences, University of São Paulo, São Paulo, Brazil, ⁶Faculty of Geosciences, University of Bremen, Bremen, Germany

Abstract Modern precipitation over northeastern (NE) South America is strongly controlled by the seasonal meridional migration of the Intertropical Convergence Zone (ITCZ). Ample evidence from the Northern Hemisphere suggests a mid- to late Holocene southward migration of the ITCZ. Such a shift would be expected to increase precipitation over semi-arid northern NE Brazil (Southern Hemisphere). However, the most robust precipitation record from northern NE Brazil shows a drying trend throughout the Holocene. Here, we address this issue presenting a high-temporal resolution reconstruction of precipitation over northern NE Brazil based on data from a marine sediment core, together with analyses of mid- and late Holocene simulations performed with the fully coupled climate model FGOALS-s2. Both, our data and the climate model simulations show a decrease in precipitation over northern NE Brazil from the mid- to the late Holocene. The model outputs further indicate a latitudinal contraction of the seasonal migration range of the ITCZ that, together with an intensification of the regional Walker circulation, were responsible for the mid- to late Holocene changes in precipitation over NE South America. Our results reconcile apparently conflicting precipitation records and climate mechanisms used to explain changes in precipitation over NE South America.

Plain Language Summary The tropical rainbelt impacts food and water security for 1 billion people. Knowing its dynamics is of utmost importance. The suggestion of a southward migration of the tropical rainbelt through the Holocene (last 11,700 years) has influenced paleoclimatology for two decades. However, most of the available evidence supporting this suggestion comes from tropical Northern Hemisphere precipitation reconstructions like northernmost South America. They systematically show a decrease in precipitation through the Holocene. In the tropical Southern Hemisphere like northeastern Brazil, at the opposite side of the tropical rainbelt, precipitation reconstructions are, however, rare. We reconstructed mid- to late Holocene (last 5,200 years) changes in precipitation over northeastern Brazil (tropical Southern Hemisphere), where modern precipitation is associated with the southern border of the tropical rainbelt. We analyzed three independent indicators of changes in precipitation recorded in marine sediments collected off northeastern Brazil. All indicators suggest a decrease in precipitation over northeastern Brazil from the mid- to the late Holocene. Together with climate model simulations, our results indicate a latitudinal contraction of the tropical rainbelt. A Holocene contraction of the rainbelt, in contrast to a southward migration, reconciles apparently conflicting precipitation reconstructions and provides valuable insights into the dynamics of the tropical rainbelt.

1. Introduction

Modern rainfall over northeastern (NE) South America is highly sensitive to and strongly controlled by the position of the Intertropical Convergence Zone (ITCZ), that is, the rising limb of the Hadley circulation (meridionally oriented overturning circulation cell) (Hastenrath, 2012; Poveda et al., 2006; Schneider et al., 2014). Today, semi-arid northern NE Brazil receives ca. 50% of its total annual precipitation during March–April, when the ITCZ and the associated equatorial precipitation reach its seasonal southernmost position over NE South America (Figure 1). A suggested mid- to late Holocene southward migration of the

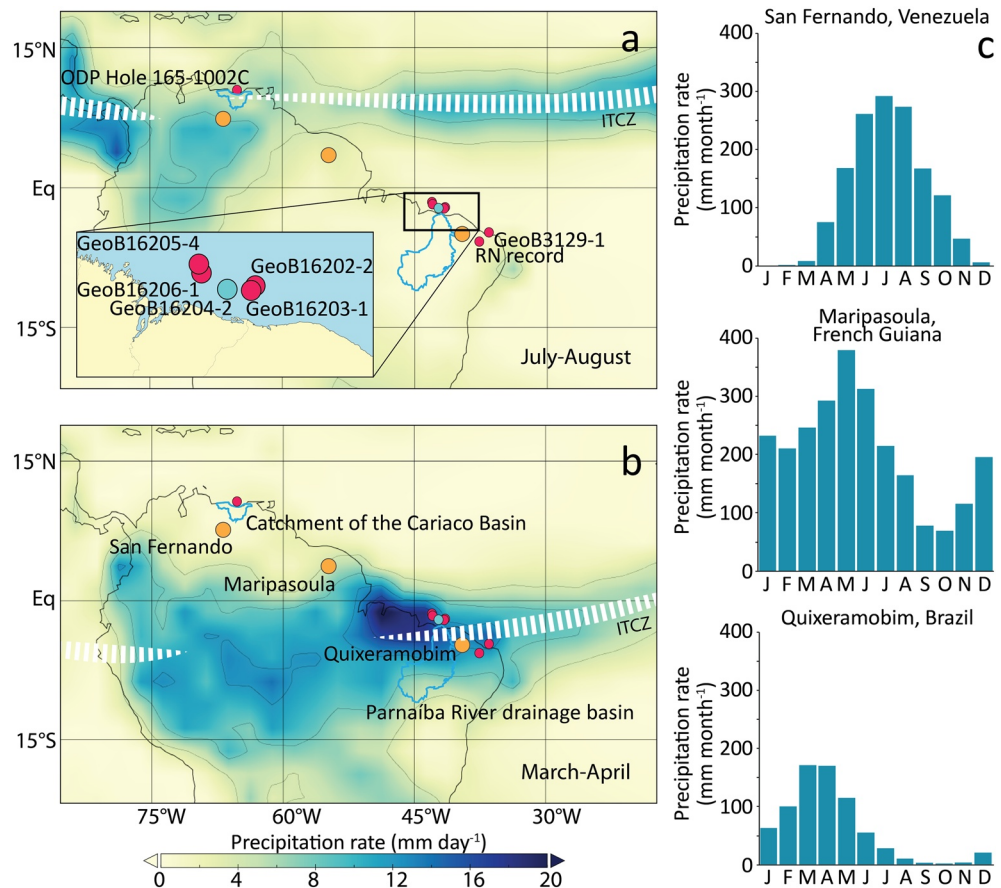


Figure 1. Study area and modern climatological precipitation. (a) Location of the main hydroclimate records discussed in the text (pink and blue circles) together with July–August precipitation (color shading) (Xie & Arkin, 1997). White dashed band schematically depicts the July–August position of the Intertropical Convergence Zone (ITCZ). The following hydroclimate records are shown (see Table 1 for details; pink circles refer to previously published records and the blue circle refers to the record investigated in this study): (i) marine sediment core ODP Hole 165–1002C from the Cariaco Basin, under the influence of local drainage basins from northernmost South America (Haug et al., 2001); (ii) marine sediment cores GeoB16205-4, GeoB16206-1, GeoB16202-2 and GeoB16203-1 off northern NE Brazil, under the influence of the Parnaíba River drainage basin (Mulitza, 2012a, 2012b; Mulitza, Chiessi, Schefuß, et al., 2017; Portilho-Ramos et al., 2017; Voigt et al., 2017; Zhang, Chiessi, Mulitza, Zabel, et al., 2015); (iii) marine sediment core GeoB16204-2 off northern NE Brazil, under the influence of the Parnaíba River drainage basin (this study); (iv) marine sediment core GeoB3129-1 off northern NE Brazil, under the influence of local drainage basins from NE Brazil (Arz et al., 1999); (v) Rainha and Furna Nova caves (RN record) in NE Brazil (Cruz et al., 2009). The orange circles depict the location of the meteorological stations that recorded the data shown in (c). The light blue outlines depict the catchment of the Cariaco Basin (northernmost South America) and the Parnaíba River drainage basin (northern NE Brazil). (b) Same as in (a) but for March–April. (c) Precipitation charts for selected long-term meteorological stations over northeastern South America for the southernmost (Quixeramobim, Brazil), central (Maripasoula, French Guiana) and northernmost (San Fernando, Venezuela) ranges of the seasonal migration of the ITCZ (T. C. Peterson & Vose, 1997). See panel (b) for the location of the meteorological stations.

ITCZ (e.g., Fleitmann et al., 2003; Haug et al., 2001; Yancheva et al., 2007) should have led to a wetting trend over northern NE Brazil. However, the only high temporal resolution and accurately dated hydroclimate record with robust hydroclimatic significance from northern NE Brazil shows a drying trend during this interval (Cruz et al., 2009). The trend was instead attributed to the intensification of the descending limb of the regional Walker circulation (zonally oriented overturning circulation cell) over northern NE Brazil, linked, in turn, to a strengthening in the center of convection over the interior of tropical South America. This raised the question of how the ITCZ behaved over NE South America from the mid- to the late Holocene. The question was furthered by the absence of a southward migration of equatorial precipitation over western Africa from the mid- to the late Holocene (Collins et al., 2011).

In order to address this issue, we analyzed the hydroclimate records archived in a high temporal resolution marine sediment core collected off northern NE Brazil adjacent to the mouth of the Parnaíba River drainage basin, and examined the mid- and late Holocene outputs of a fully coupled climate model. More specifically, we reconstructed changes in rainfall through three independent approaches: (i) bulk sediment $\ln(\text{Fe}/\text{Ca})$ and $\ln(\text{Ti}/\text{Ca})$ values (e.g., Arz et al., 1998); (ii) mass accumulation rate of the siliciclastic fraction (MAR_{sil}) (e.g., Xiong et al., 2018); and (iii) stable hydrogen isotopic composition ($\delta^2\text{H}$) of long-chain *n*-alkanes (e.g., Häggi et al., 2017). A mechanistic understanding of the reconstructed changes from our core and other NE South American ITCZ-related high temporal resolution records (Cruz et al., 2009; Haug et al., 2001) was attained by specific analyses of FGOALS-s2 climate model simulations (Bao et al., 2013).

2. Regional Setting

The hydroclimate over NE South America is mainly controlled by the meridional migration of the ITCZ (Figure 1). The ITCZ is a tropical belt of maximum precipitation resulting from deep convection (i.e., rising limb of the Hadley circulation) over the oceans (Schneider et al., 2014). Deep convection is associated with low-level convergence above the warm tropical oceans. The ITCZ controls precipitation over NE South America because of its associated vertical instability and the dominant tropical easterly winds (i.e., trade winds) that bring Atlantic moisture onto the continent (Garreaud et al., 2009). The ITCZ shows a marked seasonal meridional migration pattern, according to changes in the interhemispheric temperature gradient (i.e., following the warming hemisphere). The seasonal migration range straddles between northern NE Brazil (e.g., the Parnaíba River drainage basin) and northernmost South America (e.g., the catchment of the Cariaco Basin) (Figure 1). Accordingly, precipitation shows an unimodal yearly distribution over the southern and northern latitudinal extremes of the ITCZ, peaking during March–April over northern NE Brazil (southernmost ITCZ; exemplified by the Quixeramobim—Brazil precipitation chart in Figure 1c) (Hastenrath & Greischar, 1993), and July–August over northernmost South America (northernmost ITCZ; exemplified by the San Fernando—Venezuela precipitation chart in Figure 1c) (Poveda et al., 2006). Between these two extreme positions, precipitation shows a bimodal yearly distribution, due to the twice-yearly passages of the ITCZ (exemplified by the Maripasoula—French Guiana precipitation chart in Figure 1c). The region between these two extreme positions receives the highest annual rainfall over NE South America (Figure 1c). Northern NE Brazil, in contrast, shows a short rainy season and is characterized as a drought-prone semi-arid region (Hastenrath, 2012). Peak precipitation over northern NE Brazil and the highest Parnaíba River discharge occur in March–April, when the ITCZ occupies its southernmost position, sitting over the Parnaíba River drainage basin (Figure S1; Agência Nacional de Águas e Saneamento Básico (2000)). It is noteworthy that although the Pacific Ocean has some influence on precipitation over northern NE Brazil, Pezzi and Cavalcanti (2001) suggested that changes in the Atlantic interhemispheric sea surface temperature gradient overwhelm the influence of changes in Pacific Ocean sea surface temperatures via the strong control exerted by Atlantic sea surface temperatures over the position of the Atlantic ITCZ.

Seasonal variations in the strength of the South American monsoon system (SAMS) indirectly influence precipitation over northern NE Brazil. During austral summer, a well-developed SAMS causes abundant precipitation over western Amazonia, the central Andes and the South Atlantic Convergence Zone (SACZ) (Carvalho et al., 2004; Zhou & Lau, 1998). In the interior of tropical South America, updrafting air masses produce the upper-tropospheric Bolivian High, while the Nordeste Low is formed further east over northern NE Brazil (Lenters & Cook, 1997), setting up a regional Walker circulation. Strong deep convection over western Amazonia, the central Andes and the SACZ (typical of a strong austral summer SAMS) strengthens the descending limb of the regional Walker circulation producing large-scale subsidence and aridity over northern NE Brazil (Lenters & Cook, 1997).

Despite being dynamically linked, the ITCZ, SAMS and SACZ are independent atmospheric features controlling precipitation over distinct portions of tropical South America (Garreaud et al., 2009). Since we focus on the past behavior of the ITCZ, we exclusively rely on paleoenvironmental archives with robust hydroclimatic significance from NE South America, where precipitation is mainly controlled by the seasonal meridional migration of the ITCZ (Table 1, Figure 1). Thus, we do not consider hydroclimate archives from westernmost tropical South America and the tropical Andes where other features like the SAMS (e.g., Zhou

Table 1

Main Paleoenvironmental Archives Discussed in This Study

Archive	Latitude (°N)	Longitude (°E)	Altitude/ water depth (m)	Archive length ^a (cm)	Mean linear sedimentation rate ^a (cm kyr ⁻¹)	Step size between adjacent measurements (cm)	Type of hydroclimate record	Mean temporal resolution of hydroclimate record ^a (yr)	Reference (hydroclimate record and age model)
ODP Hole 165– 1002C	10.71	−65.17	−893	191	37	0.2	Ti	5	Haug et al. (2001)
GeoB16205- 4 ^b	−1.35	−43.09	−1955	44	9	2	ln(Fe/Ca)	216	Mulitza (2012b), Voigt et al. (2017)
GeoB16206- 1 ^b	−1.58	−43.02	−1367	45	9	3	ln(Ti/Ca)	343	Zhang, Chiessi, Mulitza, Zabel, et al. (2015), Portilho-Ramos et al. (2017)
GeoB16204-2	−2.00	−42.34	−1211	214	43	0.5	ln(Fe/Ca), ln(Ti/Ca)	12	This study
GeoB16202- 2 ^b	−1.91	−41.60	−2248	42	9	2	ln(Fe/Ca)	218	Mulitza, Chiessi, Schefuß, et al. (2017)
GeoB16203- 1 ^b	−2.03	−41.71	−1591	81	19	2	ln(Ti/Ca)	104	Mulitza (2012a), Voigt et al. (2017)
GeoB3129-1 ^b	−4.61	−36.64	−830	78	15	3	ln(Ti/Ca)	206	Arz et al. (1999)
RN record	−5.60	−37.73	100	^c	6 ^d	0.2 ^d	δ ¹⁸ O	30 ^d	Cruz et al. (2009)

^aLast 5.2 kyr. ^bAge model was recalculated by linear interpolation of calibrated radiocarbon ages in the software PaleoDataView (Langner & Mulitza, 2019) using Intcal13 (Reimer et al., 2013) and variable reservoir ages (Butzin et al., 2017). ^cNot applicable, since the RN record is composed of multiple stalagmites with different growth periods. ^dBased on Furna Nova Cave stalagmite FN1, the main stalagmite covering the last 5.2 kyr in the RN record.

& Lau, 1998), local atmospheric jets (e.g., Vera et al., 2006), topography-induced convective systems (e.g., Snow, 1976) and moisture recycling (e.g., Salati et al., 1979) also play a role.

3. Material and Methods

3.1. Marine Sediment Core Location, Description and Chronology

We investigated marine sediment core GeoB16204-2 (Table 1, Figure 1) retrieved during RV MS Merian cruise MSM20/3 (Mulitza, Chiessi, Cruz, et al., 2013) from the continental slope off northern NE Brazil. This portion of the continental slope received terrigenous sediments from the adjacent Parnaíba River drainage basin throughout the last 30 kyr (Zhang, Chiessi, Mulitza, Zabel, et al., 2015), making it ideal to track the past behavior of the ITCZ. Onboard, 1-m-long sections of core GeoB16204-2 were split longitudinally, visually described and stored at 4°C. The uppermost ca. 230 cm of core GeoB16204-2 is composed of light olive gray, gray and dark gray mud with low sand content and no evidence of depositional or erosive disturbances. A lithological change characterized by a marked decrease (increase) in reflectance (magnetic susceptibility) at ca. 230 cm core depth (Mulitza, Chiessi, Cruz, et al., 2013) may indicate a discontinuity. Hence, we focus on the uppermost 214 cm in this study. Onshore, the working half of core GeoB16204-2 was sampled twice at 2 and 2.5 cm intervals. Samples for radiocarbon and fragmentation index analyses were wet-sieved, oven-dried below 40°C, and the residues from the 150 μm size sieve were stored in glass vials and used for analyses. Hand picking of foraminiferal tests was performed under a binocular microscope. Samples for all other analyses were stored at 4°C until processing.

The age model of the uppermost 214 cm of core GeoB16204-2 is based on six accelerator mass spectrometer radiocarbon analyses performed on the shallow-dwelling planktonic foraminiferal species *Globigerinoides ruber* (pink and white) and *Globigerinoides sacculifer* (Table 2, Figure 2f). For each sample, we collected around 10 mg of CaCO₃ from the sediment fraction larger than 150 μm. Measurements were conducted at the Poznan Radiocarbon Laboratory (Poland) and the Beta Analytic Inc. (USA). All radiocarbon ages were

Table 2

Accelerator Mass Spectrometer Radiocarbon Ages and Calibrated Ages Used to Construct the Age Model of Core GeoB16204-2

Lab ID	Core depth (cm)	Species	Radiocarbon age $\pm 1\sigma$ error (yr BP)	2σ calibrated age range (cal ka BP)	Calibrated age ^a (cal ka BP)
Poz-49094	6	<i>G. ruber</i> and <i>G. sacculifer</i>	770 ± 30	0.318–0.478	0.398
Beta-350978	50	<i>G. ruber</i> and <i>G. sacculifer</i>	2120 ± 30	1.605–1.804	1.705
Beta-350979	106	<i>G. ruber</i>	3110 ± 30	2.780–2.977	2.879
Beta-350980	150	<i>G. ruber</i> and <i>G. sacculifer</i>	4030 ± 40	3.909–4.178	4.044
Poz-49095	200	<i>G. ruber</i> and <i>G. sacculifer</i>	4695 ± 35	4.831–5.024	4.928
Beta-373592	214	<i>G. ruber</i>	4880 ± 30	5.061–5.289	5.175

^aMean of the 2σ calibrated age range.

calibrated with the calibration curve Marine13 (Reimer et al., 2013) using the software Calib 7.1 (Stuiver & Reimer, 1993). All ages are indicated as calibrated thousand years before present (cal ka BP; present is 1950 AD), except where noted otherwise. The age model was obtained by the linear interpolation of the mean calibrated ages obtained from the 2σ calibrated age ranges. Importantly, a more sophisticated age-modeling approach like the Bayesian BACON tool (Blaauw & Christen, 2011) produces an age model that is virtually the same as the one obtained by linear interpolation (maximum difference of 74 years) (Figure S2).

3.2. Analyses of Major Elements

Bulk sediment Ca, Ti and Fe elemental intensities were obtained with an X-ray fluorescence (XRF) core scanner (AVAATECH serial number 12) at the MARUM—University of Bremen (Germany). Measurements were performed every 0.5 cm downcore over a 0.6 cm^2 area with downcore slit size of 0.5 cm using generator settings of 10 kV, a current of 0.065 mA, and a sampling time of 8 s directly at the split core surface of the archive half. The split core surface was covered with a $4 \mu\text{m}$ thin SPEXCerti Prep Ultralene1 foil to avoid contamination of the XRF measuring unit and desiccation of the sediment. Data were acquired by a SGX Sentsortech Silicon Drift Detector (Model SiriusSD® D65133Be-INF with 133 eV X-ray resolution), the Topaz-X High-Resolution Digital MCA, and an Oxford Instruments 100W Neptune X-ray tube with Rh target material. Raw data spectra were processed with the WinAxil software from Canberra Eurisys.

In order to quantify elemental concentrations in bulk sediment, Ca, Ti and Fe were measured via inductively coupled plasma-optical emission spectroscopy (ICP-OES) in a Varian 710 ES at the Institute of Oceanography—University of São Paulo (Brazil). Measurements were performed every ca. 4 cm downcore. Total digestion of bulk sediment samples was attained following U.S. Environmental Protection Agency (1996). Freeze-dried bulk sediment samples were pulverized in an agate mortar. Aliquots of 0.05 g of pulverized sediments were placed in Teflon digestion tubes and treated in three steps with 5 ml of HNO_3 , 2 ml of HF and 2 ml of H_2O_2 . Between each step, samples were submitted to microwave irradiation. The final solutions were analyzed via ICP-OES. An identical procedure was performed with the reference material SRM 1646a (May & Rumble, 2004). Analytical results of the reference material differ less than 2.5%, 19.0% and 6.5% ($n = 5$) from reference values (May & Rumble, 2004) for Ca, Ti and Fe, respectively. The relatively large difference between the analytical results of the reference material and the reference value for Ti is not an issue since (i) ICP-OES (and XRF-scanner) Ti and Fe show very similar changes, and (ii) the analytical results of the reference material are very close to the reference value for Fe.

Logarithms of the elemental ratios (Aitchison & Egozcue, 2005) Fe/Ca and Ti/Ca are used here as proxies for the input of continental siliciclastic material to the ocean floor (e.g., Govin, Holzwarth, et al., 2012) and, ultimately, for continental rainfall (Arz et al., 1998).

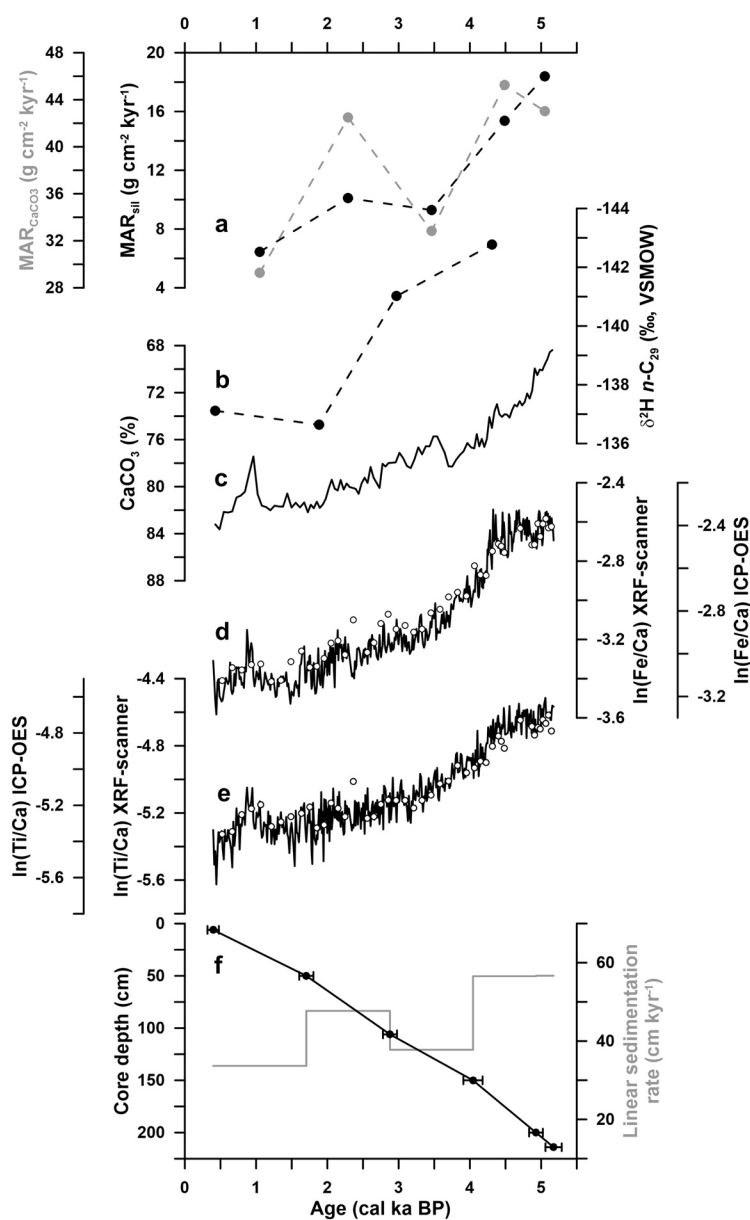


Figure 2. Downcore changes in selected physical and geochemical parameters from marine sediment core GeoB16204-2. (a) Mass accumulation rate of the siliciclastic (MAR_{sil} ; black line and black filled circles) and calcium carbonate (MAR_{CaCO_3} ; gray line and gray filled circles) fractions; (b) stable hydrogen isotopic composition (δ^2H) of C_{29} n -alkanes; (c) calcium carbonate ($CaCO_3$) content; (d) $\ln(Fe/Ca)$ obtained via X-ray fluorescence (XRF) (black line) and inductively coupled plasma-optical emission spectroscopy (ICP-OES) (open circles); (e) $\ln(Ti/Ca)$ obtained via X-ray fluorescence (XRF) (black line) and inductively coupled plasma-optical emission spectroscopy (ICP-OES) (open circles); (f) age model (black line and circles) and linear sedimentation rate (gray line). Error bars in (g) depict the 2σ calibrated age range.

3.3. Determination of Calcium Carbonate, Total Organic Carbon and Total Nitrogen Contents

The $CaCO_3$ content was determined by the weight difference prior to and after acidification of the samples following Gross (1971). Measurements were performed every ca. 2 cm downcore at the Institute of Oceanography–University of São Paulo (Brazil). Aliquots of 0.3 g of bulk sediment were treated with a 10% solution of HCl until cessation of the reaction. Results are reported as percentages of dry weight.

Total organic carbon (TOC) and total nitrogen (TN) contents were assessed via flash combustion, gas chromatography and thermal conductivity detection in a Costech ECS 4010 at the Institute of Oceanography–University of São Paulo (Brazil). Measurements were performed every ca. 2 cm downcore. Freeze-dried bulk sediment samples were pulverized in an agate mortar. Aliquots of 0.01 g of pulverized bulk sediments were placed in tin capsules for TN analyses, while aliquots of 0.01 g of pulverized decarbonated (overnight treatment with HCl) sediments were placed in tin capsules for TOC analyses. An identical procedure was performed with the reference material LECO 502-309 (LECO, 1994). Analytical results of the reference material differ less than 0.5% and 6.5% from reference values (LECO, 1994) for TOC and TN, respectively. Results are reported as percentages of dry weight.

The CaCO_3 , TOC and TN contents are used here to calculate MAR_{sil} and $\text{MAR}_{\text{CaCO}_3}$ (see Equations 1 and 2 below) (e.g., van Kreveld et al., 1996; Xiong et al., 2018).

3.4. Calculation of the Mass Accumulation Rate of the Siliciclastic and Calcium Carbonate Fractions

The MAR_{sil} and $\text{MAR}_{\text{CaCO}_3}$ were calculated based on the following equations (1 and 2, respectively):

$$\text{MAR}_{\text{sil}} = \left(1 - \left(\left(\text{CaCO}_3 + \text{TOC} + \text{TN} \right) / 100 \right) \right) * \text{LSR} * \text{DBD} \quad (1)$$

$$\text{MAR}_{\text{CaCO}_3} = \left(\text{CaCO}_3 / 100 \right) * \text{LSR} * \text{DBD} \quad (2)$$

where LSR is the linear sedimentation rate and DBD is the dry bulk density. DBD was obtained based on the following Equation 3:

$$\text{DBD} = \text{WBD} - \text{porosity} \quad (3)$$

where WBD is the wet bulk density. This assumes that (i) all pores are filled with water during the determination of WBD, and (ii) the density of water is 1 g cm^{-3} . Both, WBD and porosity were analyzed shortly after core recovery and are published in Mulitza, Chiessi, Cruz, et al. (2013). The low opal content (i.e., <1%) from Holocene sediments collected off NE South America (Mulitza, Chiessi, Schefuß, et al., 2017) together with the relatively shallow depth (i.e., 1,211 m water depth) of core GeoB16204-2 (Table 1) led us to exclude any significant influence of changes in opal content in the calculated MAR_{sil} values. MAR_{sil} and $\text{MAR}_{\text{CaCO}_3}$ values were calculated for each depth interval between two adjacent radiocarbon ages. CaCO_3 , TOC, TN, LSR, and DBD used to calculate each MAR_{sil} and $\text{MAR}_{\text{CaCO}_3}$ value are mean values for the considered depth interval. MAR_{sil} and $\text{MAR}_{\text{CaCO}_3}$ are reported in $\text{g cm}^{-2} \text{ kyr}^{-1}$.

By definition, MAR_{sil} allows quantifying the accumulation rate of continental siliciclastic material in the ocean floor and is ultimately used here as a proxy for continental rainfall (e.g., Xiong et al., 2018). $\text{MAR}_{\text{CaCO}_3}$, in turn, allows quantifying the accumulation rate of CaCO_3 in the ocean floor and is used here as a proxy for CaCO_3 productivity (e.g., van Kreveld et al., 1996) together with a planktonic foraminifera CaCO_3 productivity index (Portilho-Ramos et al., 2017).

3.5. Stable Hydrogen Isotopic Ratios From Long-Chain *n*-Alkanes

The isotopic composition of long-chain *n*-alkanes was obtained with an isotope ratio mass spectrometer (IRMS) at the MARUM—University of Bremen (Germany). Since these measurements aimed at supporting high resolution major elemental records, only four samples distributed within the uppermost 214 cm of core GeoB16204-2 were analyzed. The extraction and separation procedures of the lipids followed the same protocol as described in Häggi et al. (2016). Long-chain *n*-alkanes were quantified using a Thermo Fisher Scientific Focus gas chromatograph (GC) equipped with a Rxi-5 ms 30x column (30 m, 0.25 mm, 0.25 μm) and a flame ionization detector. Compound-specific $\delta^2\text{H}$ analyses of the C_{29} long-chain *n*-alkane was conducted on a Thermo Fisher Scientific MAT 253 IRMS coupled via a GC Isolink operated at $1,420^\circ\text{C}$ to a Thermo Fisher Scientific Trace GC equipped with an HP-5 ms column (30 m, 0.25 mm, 1 μm). $\delta^2\text{H}$ compositions were measured against calibrated H_2 reference gas and precision was controlled by external

n-alkane standards of known isotopic composition (chain length nC_{16} – nC_{34} ; isotopic composition ranging from -261 to -31 ‰; all hydrogen isotope values are given vs. VSMOW). To determine measurement precision, the difference between the measured value and the long-term mean was calculated for all standard runs conducted with the same reactor used for the samples from GeoB16204-1, yielding a 1σ error of 2.1 ‰. The H^+_3 factor during the period we performed our analyses was 5.18 , with a 1σ error of 0.02 ($n = 8$). Since we focus on the mid- and late Holocene (i.e., last ca. 5.2 kyr), no ice-volume correction was conducted.

The δ^2H composition of the C_{29} long-chain *n*-alkanes is used here as a proxy for continental rainfall (e.g., Häggi et al., 2017).

3.6. Fragmentation Index

The fragmentation index (FI (%)) of planktonic foraminifera was determined via optical microscopy with a Zeiss Stemi 2000C at the School of Arts, Sciences and Humanities–University of São Paulo (Brazil). Measurements were performed every ca. 2.5 cm downcore. Following Thunell (1976) and Conan et al. (2002), the greater than $150\ \mu m$ size fraction was split into aliquots of 300 or more planktonic foraminifera that were counted. The number of test fragments (F) and whole tests (W) were used to calculate the FI (%), as follows (4):

$$FI(\%) = F / (F + W) * 100 \quad (4)$$

A cross-calibration study comparing $CaCO_3$ preservation indexes shows that FI (%) achieved the best results (i.e., $R^2 = 0.95$) (Conan et al., 2002).

The fragmentation index is used here as a proxy for $CaCO_3$ preservation (e.g., Conan et al., 2002).

3.7. Climate Model Simulations

Mid-Holocene and preindustrial (used as the control run; represents late Holocene conditions) climatic fields from the fully coupled climate model FGOALS-s2 (Bao et al., 2013) were obtained from the PMIP3/CMIP5 database (Taylor et al., 2012). To analyze dynamical processes in the troposphere the velocity potential has been calculated at different levels by means of the inverse Laplacian of the divergence. The FGOALS-s2 was chosen against other PMIP3/CMIP5 models since it has been shown to best reproduce reconstructed mid-Holocene changes in lowland tropical South American precipitation (Figure S3) (Prado, Wainer, & Chiessi, 2013). The model appropriately simulates zonally averaged precipitation along the ITCZ, with realistic seasonal precipitation peaks with respect to time and space (see Figure 5 from Bao et al., 2013). Importantly, FGOALS-s2 correctly simulates the modern annual distribution of precipitation over northern NE Brazil with peak precipitation in March–April (Xie & Arkin, 1997), despite underestimating absolute values (Prado, Wainer, & Chiessi, 2013). The atmosphere of the FGOALS-s2 has a latitude \times longitude resolution of $1.66^\circ \times 2.81^\circ$ with 26 layers, while the ocean grid of the model has a nominal 1° resolution with grid refinement in the tropics and 30 levels (Bao et al., 2013). The mid-Holocene boundary conditions used in the model simulation include 6 ka BP orbital parameters and greenhouse gas concentrations (i.e., 280 ppm, 650 and 270 ppb for CO_2 , CH_4 and N_2O , respectively), following the PMIP3/CMIP5 protocol (Braconnot et al., 2011). Further details about the mid-Holocene PMIP3/CMIP5 experimental design are available in Harrison et al. (2015).

4. Results

4.1. Sedimentology and Geochemistry

The investigated section (i.e., uppermost 214 cm) of core GeoB16204-2 covers the last ca. 5.2 kyr with no age reversals (Table 2, Figure 2f). Linear sedimentation rates vary between ca. 34 and 57 cm kyr $^{-1}$ (mean ca. 41 cm kyr $^{-1}$), being higher (ca. 47 cm kyr $^{-1}$) during the older half of the investigated period than during the younger half (ca. 39 cm kyr $^{-1}$). Considering the sampling strategy and the linear sedimentation rates for core GeoB16204-2, the mean temporal resolution is (in the absence of bioturbation) ca. 12 years for

XRF-scanner major element analyses, ca. 96 years for ICP-OES major element analyses, ca. 48 years for CaCO_3 , TOC and TN analyses, and ca. 60 years for fragmentation index analyses.

The $\ln(\text{Fe}/\text{Ca})$ as well as the $\ln(\text{Ti}/\text{Ca})$ values generally decrease throughout the last ca. 5.2 kyr (Figures 2d and 2e; the Ca, Ti and Fe data prior to normalization are shown in Figure S4). This trend is present in both the XRF-scanner as well as the ICP-OES based data, and the strongest decrease occurs between ca. 4 and 3 cal ka BP.

The CaCO_3 content increases from ca. 70% at the bottom of the studied section of core GeoB16204-2 to ca. 85% at the top of the core (Figure 2c). TOC and TN vary in the range 0.34%–1.62% and 0.06%–0.14% (Figure S4), respectively. DBD values vary around 1.11 g cm^{-3} from 5.2 until ca. 1.5 cal ka BP, decreasing steadily after that and reaching 1.00 g cm^{-3} in the top of the core (Figure S4). MAR_{sil} and $\text{MAR}_{\text{CaCO}_3}$ values vary within the ranges $18\text{--}6 \text{ g cm}^{-2} \text{ kyr}^{-1}$ and $45\text{--}29 \text{ g cm}^{-2} \text{ kyr}^{-1}$, respectively (Figure 2a). Both records generally decrease from the base to the top of the investigated section of core GeoB16204-2, but the decrease in MAR_{sil} is proportionally larger than the decrease in $\text{MAR}_{\text{CaCO}_3}$ (52% and 19%, respectively; the two oldest and the two youngest values of each dataset were used to calculate the % change in MAR_{sil} and $\text{MAR}_{\text{CaCO}_3}$).

The $\delta^2\text{H}$ values of the C_{29} long-chain *n*-alkanes show a slight increase from ca. -143 to -137‰ upwards in core GeoB16204-2 (Figure 2b). Values of the fragmentation index vary around 56% with no long-term trend (Figure 3a).

4.2. Climate Model

The mid-Holocene FGOALS-s2 model annual mean precipitation shows a generally drier than preindustrial tropical South America with the notable exceptions of northern NE Brazil as well as northernmost South America (Figure S5). Over the tropical Atlantic, the mid-Holocene model output is characterized by increased precipitation to the north of 10°N and to the south of the equator, while drier conditions prevail between 10°N and the equator. Peak zonally (between 60°W and 0°) averaged precipitation over the tropical Atlantic and NE South America extended further south (north) during March–April (August–September) for the mid-Holocene in comparison to the preindustrial (Figures 4a and 4b). The longitudinal range $60^\circ\text{W}\text{--}0^\circ$ was chosen since it comprises the Atlantic ITCZ. Importantly, a more restrictive range (i.e., $60^\circ\text{W}\text{--}20^\circ\text{W}$) shows the same pattern. The mid-Holocene model interhemispheric surface air temperature difference (Northern Hemisphere minus Southern Hemisphere) shows positive anomalies (with respect to preindustrial) during June–September and negative anomalies during the rest of the year (Figure 4c). Regarding the lower- (upper-) troposphere wind field, anomalous convergence (divergence) characterizes the mid-Holocene equatorial South Atlantic including NE Brazil during austral summer/autumn (Figure 5).

5. Discussion

5.1. Possible Controls on the Decrease in $\ln(\text{Fe}/\text{Ca})$ and $\ln(\text{Ti}/\text{Ca})$

Considering that the transport pathway of terrigenous sediments did not changed markedly in the study area throughout the last ca. 5.2 kyr (Zhang, Chiessi, Mulitza, Zabel, et al., 2015), the decrease in our $\ln(\text{Fe}/\text{Ca})$ and $\ln(\text{Ti}/\text{Ca})$ records (Figures 2e, 2f, and 3c) could have been controlled by four processes: (i) an increase in regional relative sea-level; (ii) an increase in regional CaCO_3 productivity; (iii) an increase in CaCO_3 preservation; and (iv) a decrease in the input of continental siliciclastic material. In the marine realm far from submarine volcanoes and dust sources, Fe and Ti are typical continental-sourced elements, whereby Ca is usually marine-sourced (Govin, Holzwarth, et al., 2012). Despite its widespread use (e.g., Arz et al., 1998; Hoang et al., 2010; Revel et al., 2015), bulk sediment elemental ratios like $\ln(\text{Fe}/\text{Ca})$ and $\ln(\text{Ti}/\text{Ca})$ require careful validation in order to be adequately interpreted (e.g., Govin, Holzwarth, et al., 2012; Rothwell & Croudace, 2015). Below, we evaluate each of these four processes.

Increases in regional relative sea-level displace the coastline inland and create accommodation space on the continental shelf. As a consequence, continental siliciclastic material is preferentially trapped in the newly formed accommodation space, decreasing its delivery to the continental slope. Close to the mouth of the Parnaíba River and to our core site, however, Holocene relative sea-level reached its maximum between ca. 5.9 and 5.0 cal ka BP and decreased since then (Figure 3b) (Bezerra et al., 1998, 2003; Caldas et al., 2006).

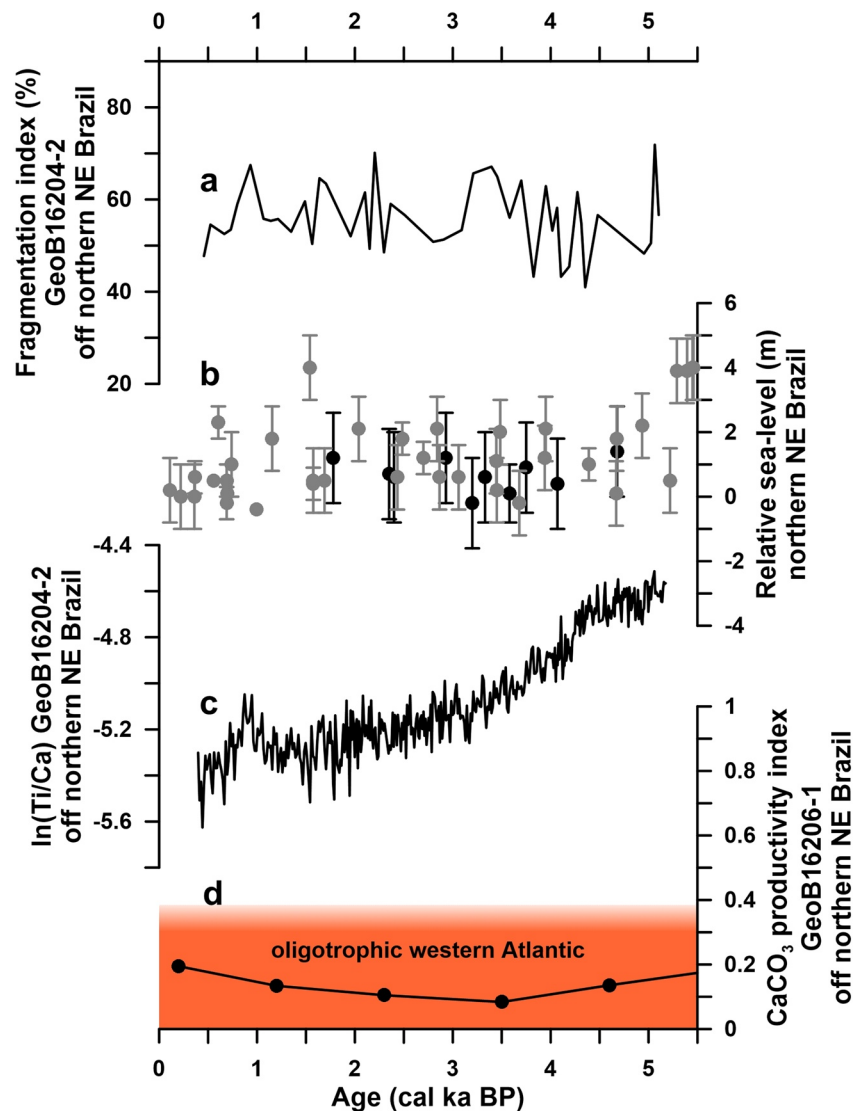


Figure 3. Downcore changes in the fragmentation and $\ln(\text{Ti}/\text{Ca})$ from marine sediment core GeoB16204-2, together with relative sea-level and CaCO_3 productivity data from the western equatorial Atlantic. (a) Fragmentation index from core GeoB16204-2 (this study). (b) Relative sea-level for northern NE Brazil From Bezerra et al. (1998) (gray symbols), Bezerra, Barreto, and Suguio (2003) (gray symbols) and Caldas et al. (2006) (black symbols). (c) $\ln(\text{Ti}/\text{Ca})$ from core GeoB16204-2 obtained via X-ray fluorescence (XRF) (this study). (d) CaCO_3 productivity index from core GeoB16206-1 (Portilho-Ramos et al., 2017) collected off northern NE Brazil near core GeoB16204-2 (Table 1, Figure 1). The CaCO_3 productivity index is defined as the sum of the abundance of the species of planktonic foraminifera adapted to high productivity conditions (i.e., *Globigerina bulloides*, *Globigerinita glutinata*, *Neogloboquadrina dutertrei*, and *Neogloboquadrina incompta*) divided by the sum of all planktonic foraminifera (Portilho-Ramos et al., 2017). The red domain highlights oligotrophic conditions typical of the western Atlantic (Garcia et al., 2019; Kucera et al., 2005).

Therefore, a decrease in relative sea-level cannot be responsible for the general decrease in our $\ln(\text{Fe}/\text{Ca})$ and $\ln(\text{Ti}/\text{Ca})$ records (Figures 2e, 2f, and 3c).

Increases in regional marine productivity enhance the flux of CaCO_3 and TOC to the ocean floor. Both enhanced fluxes dilute the concentration of continental siliciclastic material. Our study area, however, experienced no increase in productivity during the last ca. 5.2 kyr. This is shown by the low and constant values of a CaCO_3 productivity index from a nearby core (Figure 3d) (Portilho-Ramos et al., 2017), as well as by the mid- to late Holocene decrease in $\text{MAR}_{\text{CaCO}_3}$ from our core (Figure 2a). Indeed, the western equatorial Atlantic is a typically oligotrophic area (Garcia et al., 2019; Grodsky et al., 2008) and probably remained

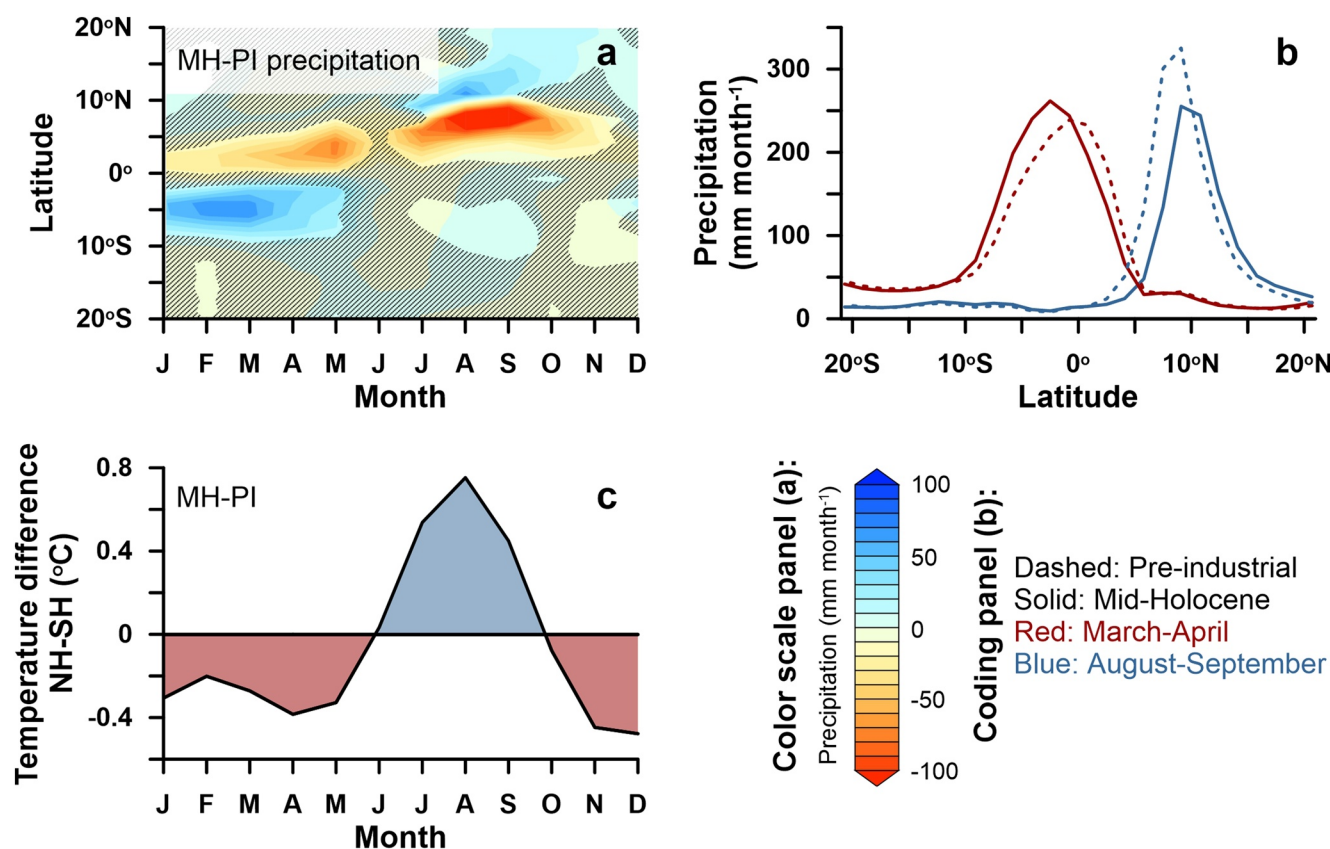


Figure 4. Precipitation and surface air temperature from the FGOALS-s2 fully coupled climate model. (a) Zonally averaged (between 60°W and 0°) mid-Holocene (MH) minus preindustrial (PI; represents late Holocene conditions) monthly precipitation. The regions where the difference in monthly precipitation is significant at the 0.05 level based on a two-tailed *t*-test are not hatched. (b) Zonally averaged (between 60°W and 0°) precipitation for March–April (August–September) in red (blue) for the mid-Holocene (preindustrial) as solid line (dashed line). (c) Mid-Holocene minus preindustrial anomaly in the surface air temperature difference between the Northern Hemisphere (NH) and the Southern Hemisphere (SH).

oligotrophic during the last ca. 5.2 kyr (Portilho-Ramos et al., 2017). Thus, changes in regional CaCO₃ productivity cannot have accounted for the general decrease in our ln(Fe/Ca) and ln(Ti/Ca) records (Figures 2e and 2f, 3c).

Increases in CaCO₃ preservation directly dilute the concentration of continental siliciclastic material. Our fragmentation index, however, suggests no long-term trend in CaCO₃ preservation throughout the last ca. 5.2 kyr (Figure 3a). The modern calcite lysocline in the western equatorial Atlantic is placed at ca. 4400 m water depth (Rühlemann et al., 1996), thus much deeper than the relatively shallow water depth (i.e., 1211 m water depth) of site GeoB16204-2. In the absence of major changes in water mass structure (Howe et al., 2016) and carbon cycle (Elsig et al., 2009) during the last ca. 5.2 kyr, the calcite lysocline is not expected to have shoaled substantially in order to affect site GeoB16204-2. Thus, changes in CaCO₃ preservation did not control the general decrease in our ln(Fe/Ca) and ln(Ti/Ca) records (Figures 2e, 2f, and 3c) throughout the last ca. 5.2 kyr.

Decreases in the input of continental siliciclastic material to the continental slope directly increase the relative concentration of marine biogenic components (e.g., CaCO₃) at the ocean floor. Thus, by exclusion, we interpret the general decrease in our ln(Fe/Ca) and ln(Ti/Ca) values (Figures 2e, 2f, and 3c) to represent a decrease in the input of continental siliciclastic material to the western equatorial Atlantic related to a decrease in fluvial input from northern NE Brazil and, more specifically, from the Parnaíba River drainage basin (Figure 1). This interpretation is corroborated by the decrease in MAR_{sil} (Figure 2a) and is supported by the C₂₉ long-chain *n*-alkane δ²H values (Figure 2b).

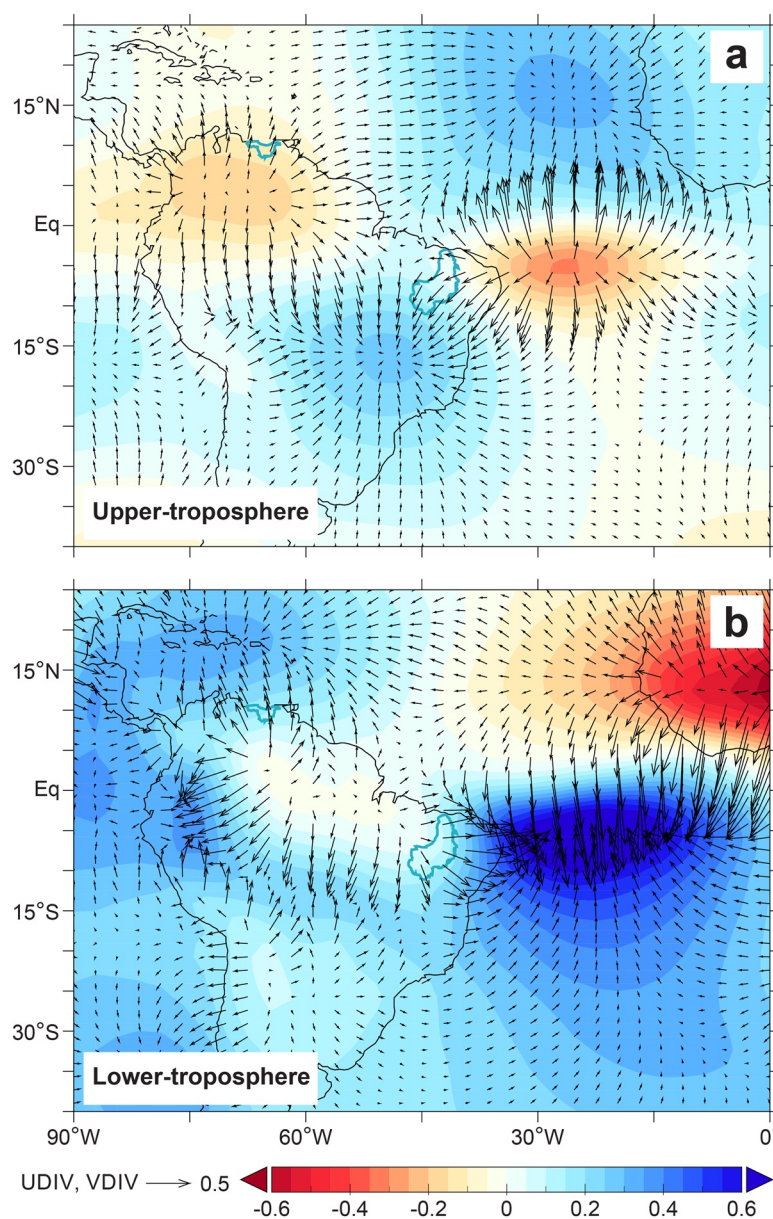


Figure 5. Velocity potential and divergent wind component from the FGOALS-s2 fully coupled climate model. (a) Mid-Holocene minus preindustrial (preindustrial represents late Holocene conditions) velocity potential ($10^6 \text{ m}^2 \text{ s}^{-1}$) and divergent wind component (m s^{-1}) for December-May (average) in the upper-troposphere at 300 hPa. The light blue outlines depict the catchment of the Cariaco Basin (northernmost South America) and the Parnaíba River drainage basin (northern NE Brazil). (b) Same as (a) but for the lower-troposphere at 925 hPa.

Slightly more enriched C_{29} long-chain n -alkane $\delta^2\text{H}$ values are present in the upper half of our core in relation to the lower half of the core (Figure 2b). Long-chain n -alkanes transported in lowland South American rivers integrate the isotopic composition of precipitation in fluvial basins (Häggi et al., 2016). The $\delta^2\text{H}$ composition of precipitation from International Atomic Energy Agency—Global Network of Isotopes in Precipitation stations over northern NE Brazil show a significant anticorrelation between precipitation $\delta^2\text{H}$ and precipitation amount (Utida et al., 2019). This pattern is induced by the amount effect that leads to lower isotopic values during periods of enhanced tropical precipitation (Dansgaard, 1964). Hence, we interpret the variations in the C_{29} long-chain n -alkane $\delta^2\text{H}$ composition in our study area to be mainly influenced by variations in precipitation amount. This suggests that the mid- to late Holocene trend toward higher $\delta^2\text{H}$

represents a decrease in mean annual precipitation indicating that the decrease in fluvial input was related to a decrease in continental precipitation.

Taken together, the new data (i.e., bulk sediment $\ln(\text{Fe}/\text{Ca})$ and $\ln(\text{Ti}/\text{Ca})$, long-chain *n*-alkane $\delta^2\text{H}$, MAR_{sil} , $\text{MAR}_{\text{CaCO}_3}$, fragmentation index; Figures 2 and 3a) from core GeoB16204-2 can most likely be explained by a decrease in fluvial input due to a decrease in continental precipitation during the last ca. 5.2 kyr. Indeed, $\ln(\text{Fe}/\text{Ca})$ and $\ln(\text{Ti}/\text{Ca})$ values from marine sediment cores collected off NE South America have been previously interpreted to be mainly controlled by changes in continental precipitation (Arz et al., 1998; Mulitza, Chiessi, Schefuß, et al., 2017; Nace et al., 2014; Zhang, Chiessi, Mulitza, Sawakuchi, et al., 2017). These previous studies, however, exclusively addressed millennial-scale changes in rainfall of the last glacial period. For the first time, we assess mid- to late Holocene changes in rainfall over NE South America based on $\ln(\text{Fe}/\text{Ca})$ and $\ln(\text{Ti}/\text{Ca})$ values from a marine sediment core.

5.2. Changes in Northeastern South American Precipitation During the Last Ca. 5.2 kyr

On the southern extreme of the modern migration range of the ITCZ over NE South America, nearly all hydroclimate records covering the last 5.2 kyr show a decrease in continental precipitation (Figures 6b–6d). Despite the lower sedimentation rate and temporal resolution for the last ca. 5.2 kyr (Table 1, Figure 1), $\ln(\text{Fe}/\text{Ca})$ and $\ln(\text{Ti}/\text{Ca})$ from other marine sediment cores (Mulitza, 2012a, 2012b; Mulitza, Chiessi, Schefuß, et al., 2017; Zhang, Chiessi, Mulitza, Zabel, et al., 2015) collected off northern NE Brazil corroborate the decrease in $\ln(\text{Fe}/\text{Ca})$ and $\ln(\text{Ti}/\text{Ca})$ from core GeoB16204-2 (Figures 6b and 6c). This is also the case for long-chain *n*-alkanes $\delta^2\text{H}$ as well as quartz and feldspar luminescence (a proxy for changes in precipitation over the Parnaíba River drainage basin) data from two nearby marine sediment cores (Mendes et al., 2019; Mulitza, Chiessi, Schefuß, et al., 2017). The sole exception to this drying trend is marine sediment core GeoB3129-1 for which $\ln(\text{Ti}/\text{Ca})$ data are inconclusive (Figures 1 and 6b) (Arz et al., 1999). In this comparison we are only considering marine sediment cores with at least one radiocarbon age within the last 5.2 kyr, no extrapolation of the age model and sedimentation rates higher than 7.5 cm kyr^{-1} (Table 1).

A similar drying trend was previously suggested for northern NE Brazil by Cruz et al. (2009) based on the RN speleothem $\delta^{18}\text{O}$ record (Figures 1 and 6d). This record stands alone in northern NE Brazil for its length, high temporal resolution, accurate dating and robust climatic significance. Records from Boqueirão Lake (coastal northern NE Brazil), for example, are too short (only spanning the last 2.3 kyr) (Utida et al., 2019) or strongly influenced by eolian and fluvial sedimentary dynamics (Viana et al., 2014; Zocatelli et al., 2012; Zular et al., 2018). Indeed, a record spanning the last 2.3 kyr is unable to record the mid- to late Holocene changes we are interested in since these changes were mostly complete before 2.5 cal ka BP (Figures 6b–6d). Records from Caçó Lake (coastal northern NE Brazil) despite suggesting a subtle drying trend throughout the Holocene (Jacob et al., 2007) may as well be influenced by eolian and fluvial sedimentary dynamics (Guedes et al., 2017; Ledru et al., 2001; Sifeddine et al., 2003; Zular et al., 2018). Thus, marine sediment core GeoB16204-2 is the first high temporal resolution hydroclimate record for northern NE Brazil (Table 1) to corroborate the drying trend throughout the mid- to late Holocene suggested by Cruz et al. (2009) (Figures 6c and 6d).

At the northern extreme of the modern migration range of the ITCZ, the Cariaco Basin Ti record also suggests a decrease in continental precipitation over the last 5.2 kyr (Figure 6a) (Haug et al., 2001). The record from Haug et al. (2001) is corroborated by other archives from northernmost South America. Two examples are the Ti and Fe data from nearby marine sediment core PL07-39PC (L. C. Peterson & Haug, 2006; Piper & Dean, 2002) as well as the multiproxy data from Valencia Lake, northern Venezuela (Curtis et al., 1999). Unfortunately, other Cariaco Basin high temporal resolution records like those analyzed by Deplazes et al. (2013) and Gibson and Peterson (2014) are not available for the late Holocene hindering a comparison to our $\ln(\text{Fe}/\text{Ca})$ and $\ln(\text{Ti}/\text{Ca})$ records. Importantly, we do not consider hydroclimate archives from the Venezuelan Andes because of their potential Pacific Ocean influence (e.g., Polissar et al., 2013).

The major drainage basins placed between the southern and northern extremes of the modern migration range of the ITCZ are the Amazon River basin and the Orinoco River basin. Hydroclimate records from the interior Amazon and Orinoco basins (e.g., Bustamante et al., 2016; Wang et al., 2017) are, however, strongly influenced by the dynamics of the SAMS (e.g., Garreaud et al., 2009; Zhou & Lau, 1998). Thus, these records

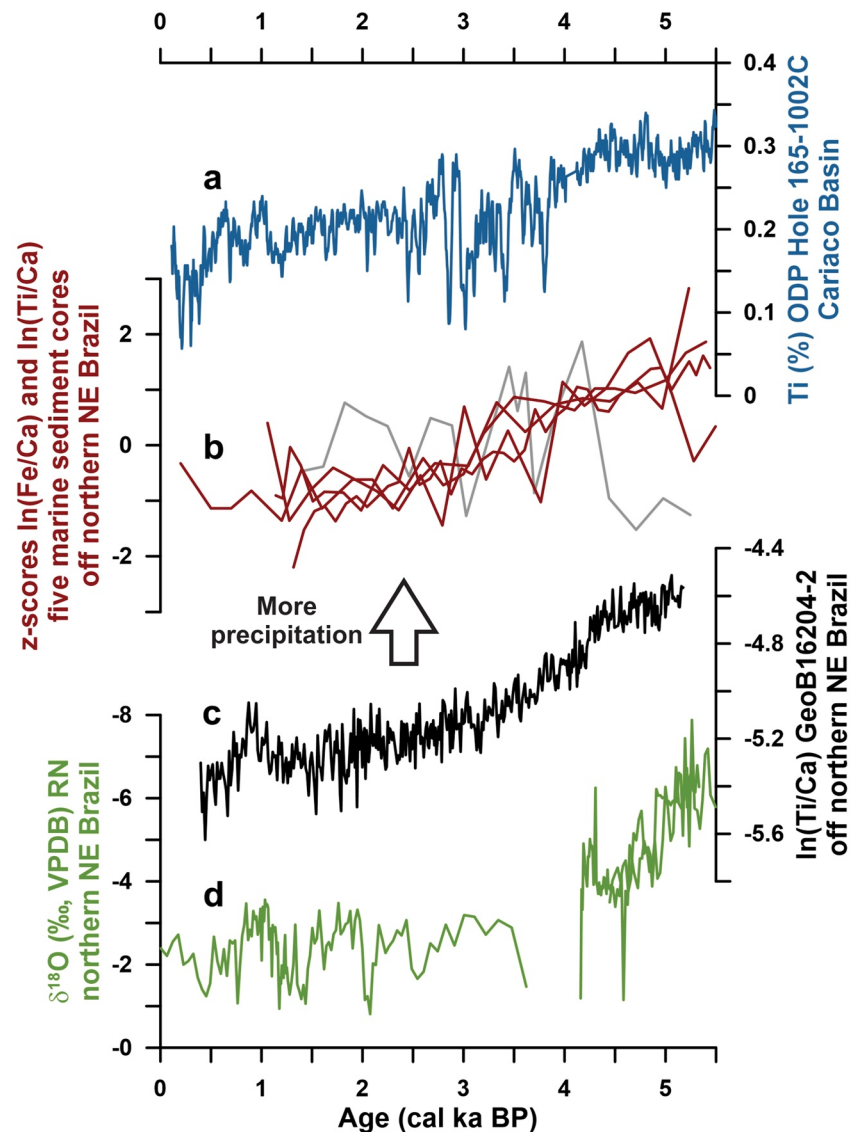


Figure 6. Main hydroclimate records from northeastern South America discussed in the text. (a) Ti content from ODP Hole 165–1002C from the Cariaco Basin, under the influence of local drainage basins from northernmost South America (Haug et al., 2001). (b) z-scores of $\ln(\text{Fe}/\text{Ca})$ or $\ln(\text{Ti}/\text{Ca})$ values from marine sediment cores collected off northern NE Brazil (all core sites under the influence of the Parnaiba River drainage basin are depicted by red lines while the core site under the influence of local northern NE Brazil drainage basins is depicted in gray): core GeoB16205-4 (red line) (Mulitza, 2012b; Voigt et al., 2017); core GeoB16206-1 (red line) (Portilho-Ramos et al., 2017; Zhang, Chiessi, Mulitza, Zabel, et al., 2015); core GeoB16202-2 (red line) (Mulitza, Chiessi, Schefuß, et al., 2017); core GeoB16203-1 (red line) (Mulitza, 2012a; Voigt et al., 2017); and core GeoB3129-1 (gray line) (Arz et al., 1999). (c) $\ln(\text{Ti}/\text{Ca})$ obtained via X-ray fluorescence (XRF) from core GeoB16204-2 collected off northern NE Brazil, under the influence of the Parnaiba River drainage basin (this study). (d) Stable oxygen isotopic composition ($\delta^{18}\text{O}$) from stalagmites of the Rainha and Furna Nova caves (RN record) in NE Brazil (Cruz et al., 2009). More information about the hydroclimate records can be found in Table 1 and Figure 1. The black arrow indicates more precipitation and is valid for all panels.

are not appropriate archives for changes in the ITCZ. A similar situation applies to hydroclimate records from marine sediment cores archiving sediments discharged by the Amazon and Orinoco Rivers (Govin, Chiessi, et al., 2014; Lund et al., 2018). The hydroclimate signals recorded in these cores are either strongly influenced by westernmost portion of the basins (Höppner et al., 2018) or show a basin-integrated signal (Häggi et al., 2016). In both situations, the SAMS dominates the hydroclimate signals making these archives not appropriate to reconstruct changes in the ITCZ. Conversely, hydroclimate archives from easternmost Amazonia recording local precipitation should be able to track changes in the ITCZ. This is to some extent

the case of the Curuá River and Akari Lake archives that indeed show a wetting trend from the mid- to the late Holocene (Behling & da Costa, 2000; Smith et al., 2011). A note of caution, however, has to be made since changes in relative sea-level on the Amazonian coast, even if of small magnitude (Cohen et al., 2012), cannot be excluded as a potential controlling factor over environmental changes recorded in these archives.

Importantly, the precipitation changes described herein over northern NE Brazil and easternmost Amazonia agree with an extensive compilation of tropical South American hydroclimate records (Prado, Wainer, Chiessi, Ledru, & Turcq, 2013). Taken together, a spatially coherent pattern of changes in precipitation over NE South America emerges for the last ca. 5.2 kyr, with a decrease in precipitation at the northern (e.g., Haug et al., 2001; L. C. Peterson & Haug, 2006) and southern (Cruz et al., 2009; this study) extremes of the ITCZ and a probable increase in its center (Behling & da Costa, 2000; Smith et al., 2011). In the next section we discuss the mechanisms that could be responsible for such changes in ITCZ-related precipitation.

5.3. Mechanisms Responsible for a Decrease in Precipitation Over Northern Northeastern Brazil During the Last Ca. 5.2 kyr

The reconstructed changes in precipitation (Figure 6) are not compatible with a simple southward migration of the ITCZ over NE South America during the mid- to the late Holocene as previously proposed (Haug et al., 2001). Instead, they are coherent with a latitudinal contraction of the seasonal migration range of the ITCZ. We suggest that the southernmost extreme of the ITCZ shifted northwards over northern NE Brazil from the mid- to the late Holocene. Concomitantly, the northernmost extreme of the ITCZ shifted southwards over northernmost South America. This accommodates all precipitation reconstructions from NE South America that cover the last 5.2 kyr, show high temporal resolution, are accurately dated and are robustly controlled by the ITCZ (Table 1, Figures 1 and 6).

The FGOALS-s2 model results support one such latitudinal contraction of the seasonal migration range of the ITCZ from the mid- to the late Holocene (Figures 4a and 4b). While peak tropical precipitation during March–April (the period when the ITCZ reaches its southernmost position) shifted northwards from 2.5°S–0.8°S to 0.8°S–0.8°N, peak precipitation during August–September (the period when the ITCZ reaches its northernmost position) migrated southwards from 10.8°N–9.1°N to 9.1°N–7.5°N from the mid- to the late Holocene (Figure 4b). The position of the ITCZ is strongly coupled to the interhemispheric temperature gradient (Schneider et al., 2014). Indeed, the extended seasonal range of the ITCZ that characterized the mid-Holocene is explained by a negative anomaly in the interhemispheric surface air temperature difference during March–April (i.e., a relative warming of the South Atlantic in relation to the North Atlantic) and a positive anomaly during August–September (i.e., a relative warming of the North Atlantic in relation to the South Atlantic) compared to the late Holocene (Figure 4c). These changes in the interhemispheric temperature gradient mainly resulted from the differential response of both hemispheres to seasonal changes in orbital insolation, because of the different proportion of continental versus oceanic areas in both hemispheres and its control over thermal inertia. Further mechanisms that specifically contribute to the formation of an anomalous meridional surface temperature gradient in the tropical Atlantic were discussed elsewhere (Zhao et al., 2005).

Interestingly, Cruz et al. (2009) proposed a different mechanism to explain the wetter northern NE Brazil during the mid-Holocene relative to the late Holocene, namely a weakening of the descending limb of the regional Walker circulation over northern NE Brazil associated with a weaker SAMS (e.g., Prado, Wainer, Chiessi, Ledru, & Turcq, 2013). We further tested this mechanism with the FGOALS-s2 model outputs and found it to work in parallel to the latitudinal contraction of the ITCZ. During the northern NE Brazil wet season (austral summer/autumn) the model simulates a mid-Holocene anomalous upper-troposphere divergence over the western equatorial South Atlantic and northern NE Brazil linked to a weakening of the Nordeste Low, while in the lower-troposphere an anomalous convergent flow is found (Figure 5). Part of the anomalous outflow from the upper-troposphere divergent region, which is linked to enhanced deep convection and rainfall, is directed northward and balanced by an anomalous lower-troposphere southward flow associated with an ITCZ that seasonally reaches further south during the mid-Holocene. Another part of the anomalous outflow from the upper-troposphere divergent region has a zonal component and is directed toward the South American continent, where anomalous upper-troposphere convergence is linked to reduced deep convection in a weaker SAMS resulting from lower seasonal insolation. Thus, the model

results support the occurrence of two mechanisms that were responsible for mid- to late Holocene precipitation changes over NE South America: (i) latitudinal contraction of the seasonal migration range of the ITCZ; and (ii) strengthening of the descending limb of the regional Walker circulation. Importantly, both mechanisms operated together and are, to some extent, related to each other through lower- and upper-tropospheric circulation features.

Analyzing the tropical South American output for mid-Holocene climate simulations from the PMIP3/CMIP5, Prado, Wainer, and Chiessi (2013) showed that seven out of the eight analyzed models simulated a wetter northern NE Brazil during the mid-Holocene relative to the late Holocene. The authors, however, did not scrutinize the mechanisms responsible for that anomaly, as performed herewith. Investigating an atmosphere-only general circulation model, Maksic et al. (2019) also suggested that northern NE Brazil was wetter during the mid-Holocene in relation to the late Holocene, and added that this occurred because of an extended seasonal southward migration of the ITCZ during the mid-Holocene. Through a sensitivity experiment, the authors concluded that changes in sea-surface temperatures were responsible for the extended seasonal southward migration. Exploring the SAMS dynamics during the mid-Holocene in 10 PMIP3/CMIP5 models [not including the FGOALS-s2 model that outperformed other PMIP3/CMIP5 models in reproducing mid-Holocene changes in lowland tropical South American precipitation (Prado, Wainer, & Chiessi, 2013)], Shimizu et al. (2020) showed that the weaker mid-Holocene SAMS controlled the increased precipitation over northern NE Brazil. More specifically, the authors associated the wetter mid-Holocene northern NE Brazil with a weakening of the regional Walker circulation. Thus, our results are not in contradiction to Prado, Wainer, and Chiessi (2013), Maksic et al. (2019), and Shimizu et al. (2020), instead they are complementary to those studies.

As a side note, we consider unlikely that precipitation directly related to the SACZ influenced precipitation changes over northern NE Brazil from the mid- to the late Holocene. Indeed, in modern climate, the SACZ is placed at ca. 20°S at the longitude of the Parnaíba River drainage basin (Carvalho et al., 2004). Also, the SACZ shows little meridional displacement (Liebmann et al., 1999). Since the Parnaíba River drainage basin only extends to ca. 10°S (Figures 1a and 1b), a putative direct effect of the SACZ over the Parnaíba River drainage basin would require a substantial northward displacement of the SACZ that is difficult to accomplish (Carvalho et al., 2004). Moreover, if the SACZ would have migrated to 10°S (at the longitude of the Parnaíba River drainage basin) during the mid-Holocene, other robust eastern South American precipitation records collected to the south of the Parnaíba River drainage basin would also have registered this displacement. The highest resolved hydroclimate record that fulfills this condition, a speleothem $\delta^{18}\text{O}$ record from eastern Brazil, does not show any sign of a mid- to late Holocene orbital change (Strikis et al., 2011). Thus, we do not consider that a northward migration of the SACZ was responsible for the increased mid-Holocene precipitation over the Parnaíba River drainage basin.

Finally, together with Collins et al. (2011) our results suggest a mid- to late Holocene latitudinal contraction of equatorial precipitation on both sides of the Atlantic, challenging the hypothesis of a southward migration of the Atlantic ITCZ during that time. The contraction, in contrast to a southward migration, would require no major change in annual cross-equatorial atmospheric (accomplished by the Hadley circulation) and oceanic [accomplished by the Atlantic meridional overturning circulation (AMOC)] heat transport (Marshall et al., 2014), satisfying the absence of substantial long-term changes in AMOC strength during the last ca. 5.2 kyr (Lippold et al., 2019).

6. Conclusions

Our new data (i.e., bulk sediment $\ln(\text{Fe}/\text{Ca})$ and $\ln(\text{Ti}/\text{Ca})$, MAR_{sil} , $\text{MAR}_{\text{CaCO}_3}$, long-chain *n*-alkane $\delta^2\text{H}$, and fragmentation index), together with previously published regional relative sea level and CaCO_3 productivity records, show that precipitation over northern NE Brazil decreased from the mid- to the late Holocene. A compilation of paleoenvironmental records with robust hydroclimatic significance from NE South America shows that precipitation decreased not only over northern NE Brazil (i.e., the southernmost seasonal extreme of the ITCZ) but also over northernmost South America (i.e., the northernmost seasonal extreme of the ITCZ) during the same period. The available paleoenvironmental records between these two extreme positions are less conclusive but suggest a mid- to late Holocene precipitation increase. This pattern of

changes in precipitation suggests a latitudinal contraction of the seasonal migration range of the ITCZ over NE South America from the mid- to the late Holocene. Our model analyses corroborate the latitudinal contraction of the ITCZ and link it to orbital insolation-driven changes in the interhemispheric surface temperature difference. In addition, our model analyses suggest that a mid- to late Holocene intensification of atmospheric zonal circulation (regional Walker circulation) linked to a strengthening of the SAMS also contributed to the drying trend over northern NE Brazil. Our results reconcile apparently conflicting precipitation records and mechanisms, challenging the hypothesis of a southward migration of the Atlantic ITCZ through the Holocene.

Data Availability Statement

The new data shown herein are available in Pangaea (<https://doi.pangaea.de/10.1594/PANGAEA.921255>).

Acknowledgments

The authors thank three anonymous reviewers as well as the associate editor and the editor for constructive comments that greatly improved the paper. C.M. Chiessi acknowledges the financial support from FAPESP (grants 2018/15123-4, 2019/10642-6 and 2019/24349-9), CAPES (grants 564/2015 and 88881.313535/2019-01), CNPq (grants 302607/2016-1 and 312458/2020-7) and the Alexander von Humboldt Foundation. N.K. Taniguchi acknowledges the financial support from FAPESP (grants 2013/10676-1 and 2013/26954-1). M. Prange acknowledges support from the BMBF PalMod initiative. M.C. Campos acknowledges the financial support from FAPESP (grants 2016/10242-0 and 2018/06790-7). R.C. Portillo-Ramos acknowledges the financial support from the European Union's Horizon 2020 iAtlantic project (Grant 818123). S.H.M. Sousa acknowledges the financial support from CNPq (Grant 307341/2018-6). Logistic and technical assistance was provided by the captain and crew of the RV MS Merian. The authors acknowledge the GeoB Core Repository at MARUM—University of Bremen for supplying the samples used in this study. The authors thank the PMIP community for sharing climate model output, as well as Márcia C. Bicego and Rubens C.L. Figueira for assistance with TOC + TN and ICP-OES analyses, respectively. This research used data acquired at the XRF Core Scanner Lab at the MARUM—Center for Marine Environmental Sciences, University of Bremen, Germany.

References

- Agência Nacional de Águas e Saneamento Básico. (2000). *Hidroweb: Sistema de Informações Hidrológicas*. Retrieved from <http://www.snirh.gov.br/hidroweb/>
- Aitchison, J., & J. Egozcue, J. (2005). Compositional data analysis: Where are we and where should we be heading? *Mathematical Geosciences*, 37(7), 829–850. <https://doi.org/10.1007/s11004-005-7383-7>
- Arz, H. W., Pätzold, J., & Wefer, G. (1998). Correlated millennial-scale changes in surface hydrography and terrigenous sediment yield inferred from last-glacial marine deposits off northeastern Brazil. *Quaternary Research*, 50(2), 157–166. <https://doi.org/10.1006/qres.1998.1992>
- Arz, H. W., Pätzold, J., & Wefer, G. (1999). Climatic changes during the last deglaciation recorded in sediment cores from the northeastern Brazilian Continental Margin. *Geo-Marine Letters*, 19(3), 209–218. <https://doi.org/10.1007/s003670050111>
- Bao, Q., Lin, P., Zhou, T., Liu, Y., Yu, Y., Wu, G., et al. (2013). The Flexible Global Ocean-Atmosphere-Land system model, Spectral Version 2: FGOALS-s2. *Advances in Atmospheric Sciences*, 30(3), 561–576. <https://doi.org/10.1007/s00376-012-2113-9>
- Behling, H., & da Costa, M. L. (2000). Holocene Environmental Changes from the Rio Curuá Record in the Caxiuanã Region, Eastern Amazon Basin. *Quaternary Research*, 53(3), 369–377. <https://doi.org/10.1006/qres.1999.2117>
- Bezerra, F. H. R., Barreto, A. M. F., & Suguio, K. (2003). Holocene sea-level history on the Rio Grande do Norte State coast, Brazil. *Marine Geology*, 196(1–2), 73–89. [https://doi.org/10.1016/S0025-3227\(03\)00044-6](https://doi.org/10.1016/S0025-3227(03)00044-6)
- Bezerra, F. H. R., Lima-Filho, F. P., Amaral, R. F., Caldas, L. H. O., & Costa-Neto, L. X. (1999). Holocene coastal tectonics in NE Brazil. *Geological Society, London, Special Publications*, 146(1), 279–293. <https://doi.org/10.1144/gsl.sp.1999.146.01.17>
- Blaauw, M., & Christen, J. A. (2011). Flexible paleoclimate age-depth models using an autoregressive gamma process. *Bayesian Analysis*, 6(3), 457–474. <https://doi.org/10.1214/11-BA61810.1214/ba/1339616472>
- Braconnot, P., Harrison, S. P., Otto-Bliesner, B., Abe-Ouchi, A., Jungclauss, J., & Peterschmitt, J. Y. (2011). The Paleoclimate Modeling Intercomparison Project contribution to CMIP5. *CLIVAR Exchanges*, 56, 15–19.
- Bustamante, M. G., Cruz, F. W., Vuille, M., Apaestegui, J., Strikis, N., Panizo, G., et al. (2016). Holocene changes in monsoon precipitation in the Andes of NE Peru based on $\delta^{18}\text{O}$ speleothem records. *Quaternary Science Reviews*, 146, 274–287. <https://doi.org/10.1016/j.quascirev.2016.05.023>
- Butzin, M., Köhler, P., & Lohmann, G. (2017). Marine radiocarbon reservoir age simulations for the past 50,000 years. *Geophysical Research Letters*, 44, 8473–8480. <https://doi.org/10.1002/2017GL074688>
- Caldas, L. H. D. O., Stattegger, K., & Vital, H. (2006). Holocene sea-level history: Evidence from coastal sediments of the northern Rio Grande do Norte coast, NE Brazil. *Marine Geology*, 228(1), 39–53. <https://doi.org/10.1016/j.margeo.2005.12.008>
- Carvalho, L. M. V., Jones, C., & Liebmann, B. (2004). The South Atlantic Convergence Zone: Intensity, form, persistence, and relationships with intraseasonal to interannual activity and extreme rainfall. *Journal of Climate*, 17, 88–108. [https://doi.org/10.1175/1520-0442\(2004\)017<0088:TSACZ>2.0.CO;2](https://doi.org/10.1175/1520-0442(2004)017<0088:TSACZ>2.0.CO;2)
- Cohen, M. C. L., Pessenda, L. C. R., Behling, H., de Fátima Rossetti, D., França, M. C., Guimarães, J. T. F., et al. (2012). Holocene paleoenvironmental history of the Amazonian mangrove belt. *Quaternary Science Reviews*, 55, 50–58. <https://doi.org/10.1016/j.quascirev.2012.08.019>
- Collins, J. A., Schefuß, E., Heslop, D., Mulitza, S., Prange, M., Zabel, M., et al. (2011). Interhemispheric symmetry of the tropical African rainbelt over the past 23,000 years. *Nature Geoscience*, 4(1), 42–45. <https://doi.org/10.1038/ngeo1039>
- Conan, S. M.-H., Ivanova, E. M., & Brummer, G.-J. A. (2002). Quantifying carbonate dissolution and calibration of foraminiferal dissolution indices in the Somali Basin. *Marine Geology*, 182(3), 325–349. [https://doi.org/10.1016/S0025-3227\(01\)00238-9](https://doi.org/10.1016/S0025-3227(01)00238-9)
- Cruz, F. W., Vuille, M., Burns, S. J., Wang, X., Cheng, H., Werner, M., et al. (2009). Orbitally driven east-west antiphasing of South American precipitation. *Nature Geoscience*, 2(3), 210–214. <https://doi.org/10.1038/ngeo444>
- Curtis, J. H., Brenner, M., & Hodel, D. A. (1999). Climate change in the Lake Valencia Basin, Venezuela, ~12600 yr BP to present. *The Holocene*, 9(5), 609–619. <https://doi.org/10.1191/09596839969724431>
- Dansgaard, W. (1964). Stable isotopes in precipitation. *Tellus*, 16(4), 436–468. <https://doi.org/10.1111/j.2153-3490.1964.tb00181.x10.3402/tellusa.v16i4.8993>
- Deplazes, G., Lückge, A., Peterson, L. C., Timmermann, A., Hamann, Y., Huguén, K. A., et al. (2013). Links between tropical rainfall and North Atlantic climate during the last glacial period. *Nature Geoscience*, 6(3), 213–217. <https://doi.org/10.1038/ngeo1712>
- Elsig, J., Schmitt, J., Leuenberger, D., Schneider, R., Eyer, M., Leuenberger, M., et al. (2009). Stable isotope constraints on Holocene carbon cycle changes from an Antarctic ice core. *Nature*, 461(7263), 507–510. <https://doi.org/10.1038/nature08393>
- Fleitmann, D., Burns, S. J., Mudelsee, M., Neff, U., Kramers, J., Mangini, A., et al. (2003). Holocene forcing of the Indian monsoon recorded in a stalagmite from southern Oman. *Science*, 300(5626), 1737–1739. <https://doi.org/10.1126/science.1083130>
- García, H. E., Weathers, K. W., Paver, C. R., Smolyar, I., Boyer, T. P., Locarnini, R. A., et al. (2019). *World Ocean Atlas 2018. Vol. 4: Dissolved Inorganic Nutrients (phosphate, nitrate and nitrate+nitrite, silicate)*. In A. V. Mishonov (Ed.), (pp. 35). Silver Spring, MD.

- Garreaud, R. D., Vuille, M., Compagnucci, R., & Marengo, J. (2009). Present-day South American climate. *Palaeogeography, Palaeoclimatology, Palaeoecology*, 281(3–4), 180–195. <https://doi.org/10.1016/j.palaeo.2007.10.032>
- Gibson, K. A., & Peterson, L. C. (2014). A 0.6 million year record of millennial-scale climate variability in the tropics. *Geophysical Research Letters*, 41, 969–975. <https://doi.org/10.1002/2013GL058846>
- Govin, A., Chiessi, C. M., Zabel, M., Sawakuchi, A. O., Heslop, D., Hörner, T., et al. (2014). Terrigenous input off northern South America driven by changes in Amazonian climate and the North Brazil Current retroflexion during the last 250 ka. *Climate of the Past*, 10(2), 843–862. <https://doi.org/10.5194/cp-10-843-2014>
- Govin, A., Holzwarth, U., Heslop, D., Ford Keeling, L., Zabel, M., Mulitza, S., et al. (2012). Distribution of major elements in Atlantic surface sediments (36°N–49°S): Imprint of terrigenous input and continental weathering. *Geochemistry, Geophysics, Geosystems*, 13, Q01013. <https://doi.org/10.1029/2011gc003785>
- Grodsky, S. A., Carton, J. A., & McClain, C. R. (2008). Variability of upwelling and chlorophyll in the equatorial Atlantic. *Geophysical Research Letters*, 35, L03610. <https://doi.org/10.1029/2007gl032466>
- Gross, M. G. (1971). Carbon determination. In R. E. Carver, (Ed.), *Procedures in sedimentary Petrology* (pp. 573–596). New York, NY: Wiley-Interscience
- Guedes, C. C. F., Giannini, P. C. F., Sawakuchi, A. O., DeWitt, R., & Aguiar, V. A. P. (2017). Weakening of northeast trade winds during the Heinrich stadial 1 event recorded by dune field stabilization in tropical Brazil. *Quaternary Research*, 88(3), 369–381. <https://doi.org/10.1017/qua.2017.79>
- Häggi, C., Chiessi, C. M., Merkel, U., Mulitza, S., Prange, M., Schulz, M., & Schefuß, E. (2017). Response of the Amazon rainforest to late Pleistocene climate variability. *Earth and Planetary Science Letters*, 479, 50–59. <https://doi.org/10.1016/j.epsl.2017.09.013>
- Häggi, C., Sawakuchi, A. O., Chiessi, C. M., Mulitza, S., Mollenhauer, G., Sawakuchi, H. O., et al. (2016). Origin, transport and deposition of leaf-wax biomarkers in the Amazon Basin and the adjacent Atlantic. *Geochimica et Cosmochimica Acta*, 192, 149–165. <https://doi.org/10.1016/j.gca.2016.07.002>
- Harrison, S. P., Bartlein, P. J., Izumi, K., Li, G., Annan, J., Hargreaves, J., et al. (2015). Evaluation of CMIP5 palaeo-simulations to improve climate projections. *Nature Climate Change*, 5(8), 735–743. <https://doi.org/10.1038/nclimate2649>
- Hastenrath, S. (2012). Exploring the climate problems of Brazil's Nordeste: a review. *Climatic Change*, 112(2), 243–251. <https://doi.org/10.1007/s10584-011-0227-1>
- Hastenrath, S., & Greischar, L. (1993). Circulation mechanisms related to northeast Brazil rainfall anomalies. *Journal of Geophysical Research*, 98(D3), 5093–5102. <https://doi.org/10.1029/92jd02646>
- Haug, G. H., Hughen, K. A., Sigman, D. M., Peterson, L. C., & Rohl, U. (2001). Southward migration of the intertropical convergence zone through the Holocene. *Science*, 293(5533), 1304–1308. <https://doi.org/10.1126/science.1059725>
- Hoang, L., Clift, P., Schwab, A., Huuse, M., Nguyen, D., & Sun, Z. (2010). Large-scale Erosional Response of SE Asia to Monsoon Evolution Reconstructed From Sedimentary Records of the Song Hong-Yinggehai and Qiongdongnan Basins, South China Sea. *Geological Society, London, Special Publications*, 342, 219–244. <https://doi.org/10.1144/SP342.13>
- Höppner, N., Lucassen, F., Chiessi, C. M., Sawakuchi, A. O., & Kasemann, S. A. (2018). Holocene provenance shift of suspended particulate matter in the Amazon River basin. *Quaternary Science Reviews*, 190, 66–80. <https://doi.org/10.1016/j.quascirev.2018.04.021>
- Howe, J. N. W., Piotrowski, A. M., Oppo, D. W., Huang, K.-F., Mulitza, S., Chiessi, C. M., & Blusztajn, J. (2016). Antarctic intermediate water circulation in the South Atlantic over the past 25,000 years. *Paleoceanography*, 31, 1302. PA002975. <https://doi.org/10.1002/2016PA002975>
- Jacob, J., Huang, Y., Disnar, J.-R., Sifeddine, A., Boussafir, M., Spadano Albuquerque, A. L., & Turcq, B. (2007). Paleohydrological changes during the last deglaciation in Northern Brazil. *Quaternary Science Reviews*, 26(7–8), 1004–1015. <https://doi.org/10.1016/j.quascirev.2006.12.004>
- Kucera, M., Weinelt, M., Kiefer, T., Pflaumann, U., Hayes, A., Weinelt, M., et al. (2005). Reconstruction of sea-surface temperatures from assemblages of planktonic foraminifera: multi-technique approach based on geographically constrained calibration data sets and its application to glacial Atlantic and Pacific Oceans. *Quaternary Science Reviews*, 24(7–9), 951–998. <https://doi.org/10.1016/j.quascirev.2004.07.014>
- Langner, M., & Mulitza, S. (2019). Technical note: PaleoDataView - a software toolbox for the collection, homogenization and visualization of marine proxy data. *Climate of the Past*, 15(6), 2067–2072. <https://doi.org/10.5194/cp-15-2067-2019>
- LECO. (1994). *LECO calibration sample Certificate of Traceability - 502-309*. St. Joseph, MI: LECO.
- Ledru, M.-P., Cordeiro, R. C., Dominguez, J. M. L., Martin, L., Mourguiart, P., Sifeddine, A., & Turcq, B. (2001). Late-Glacial Cooling in Amazonia Inferred from Pollen at Lagoa do Caçó, Northern Brazil. *Quaternary Research*, 55(1), 47–56. <https://doi.org/10.1006/qres.2000.2187>
- Lenters, J. D., & Cook, K. H. (1997). On the origin of the Bolivian high and related circulation features of the south American climate. *Journal of the Atmospheric Sciences*, 54(5), 656–678. [https://doi.org/10.1175/1520-0469\(1997\)054<0656:OTOOTB>2.0.CO;2](https://doi.org/10.1175/1520-0469(1997)054<0656:OTOOTB>2.0.CO;2)
- Liebmann, B., Kiladis, G. N., Marengo, J., Ambrizzi, T., & Glick, J. D. (1999). Submonthly convective variability over south America and the south Atlantic convergence zone. *Journal of Climate*, 12(7), 1877–1891. [https://doi.org/10.1175/1520-0442\(1999\)012<1877:SCVO-SA>2.0.CO;2](https://doi.org/10.1175/1520-0442(1999)012<1877:SCVO-SA>2.0.CO;2)
- Lippold, J., Pöppelmeier, F., Süfke, F., Gutjahr, M., Goepfert, T. J., Blaser, P., et al. (2019). Constraining the variability of the Atlantic meridional overturning circulation during the holocene. *Geophysical Research Letters*, 46, 11338–11346. <https://doi.org/10.1029/2019gl084988>
- Lund, S., Mortazavi, E., Chong, L., Platzman, E., & Berelson, W. (2018). Holocene sedimentation on the distal Amazon Fan/Demerara Abyssal Plain. *Marine Geology*, 404, 147–157. <https://doi.org/10.1016/j.margeo.2018.06.015>
- Maksic, J., Shimizu, M. H., de Oliveira, G. S., Venancio, I. M., Cardoso, M., & Ferreira, F. A. (2019). Simulation of the Holocene climate over South America and impacts on the vegetation. *The Holocene*, 29(2), 287–299. <https://doi.org/10.1177/0959683618810406>
- Marshall, J., Donohoe, A., Ferreira, D., & McGee, D. (2014). The ocean's role in setting the mean position of the Inter-Tropical Convergence Zone. *Climate Dynamics*, 42(7), 1967–1979. <https://doi.org/10.1007/s00382-013-1767-z>
- May, W. E., & Rumble, J. (2004). *Certificate of Analysis - standard reference material 1646a - Estuarine sediment* (pp. 1–4). Gaithersburg, MD: National Institute of Standards and Technology. Retrieved from <https://www-s.nist.gov/srmors/certificates/1646A.pdf>
- Mendes, V. R., Sawakuchi, A. O., Chiessi, C. M., Giannini, P. C. F., Rehfeld, K., & Mulitza, S. (2019). Thermoluminescence and optically stimulated luminescence measured in marine sediments indicate precipitation changes over northeastern Brazil. *Paleoceanography and Paleoclimatology*, 34(8), 1476–1486. <https://doi.org/10.1029/2019pa003691>
- Mulitza, S. (2012a). *X-ray fluorescence wet sample measurements of MSM20/3 sediment core GeoB16203-1*. Retrieved from <https://doi.pangaea.de/10.1594/PANGAEA.785982>
- Mulitza, S. (2012b). *X-ray fluorescence wet sample measurements of MSM20/3 sediment core GeoB16205-4*. Retrieved from <https://doi.pangaea.de/10.1594/PANGAEA.786005>

- Mulitza, S., Chiessi, C. M., Cruz, A. P. S., Frederichs, T., Gomes, J. G., Gurgel, M., et al. (2013). *Response of Amazon sedimentation to deforestation, land use and climate variability – Cruise No. MSM20/3 – February 19 – March 11, 2012 – Recife (Brazil) – Bridgetown (Barbados)*, MARIA S. MERIAN-Berichte (pp. 1–86). DFG-Senatskommission für Ozeanographie. https://doi.org/10.2312/cr_msm20_3
- Mulitza, S., Chiessi, C. M., Schefuß, E., Lippold, J., Wichmann, D., Antz, B., et al. (2017). Synchronous and proportional deglacial changes in Atlantic meridional overturning and northeast Brazilian precipitation. *Paleoceanography*, 32(6), 622. PA003084. <https://doi.org/10.1002/2017PA003084>
- Nace, T. E., Baker, P. A., Dwyer, G. S., Silva, C. G., Rigsby, C. A., Burns, S. J., et al. (2014). The role of North Brazil Current transport in the paleoclimate of the Brazilian Nordeste margin and paleoceanography of the western tropical Atlantic during the late Quaternary. *Paleogeography, Palaeoclimatology, Palaeoecology*, 415(0), 3–13. <https://doi.org/10.1016/j.palaeo.2014.05.030>
- Peterson, L. C., & Haug, G. H. (2006). Variability in the mean latitude of the Atlantic Intertropical Convergence Zone as recorded by riverine input of sediments to the Cariaco Basin (Venezuela). *Paleogeography, Palaeoclimatology, Palaeoecology*, 234(1), 97–113. <https://doi.org/10.1016/j.palaeo.2005.10.021>
- Peterson, T. C., & Vose, R. S. (1997). An overview of the global historical climatology network temperature database. *Bulletin of the American Meteorological Society*, 78(12), 2837–2849. [https://doi.org/10.1175/1520-0477\(1997\)078<2837:aootgh>2.0.co;2](https://doi.org/10.1175/1520-0477(1997)078<2837:aootgh>2.0.co;2)
- Pezzi, L., & Cavalcanti, I. (2001). The relative importance of ENSO and tropical Atlantic sea surface temperature anomalies for seasonal precipitation over South America: A numerical study. *Climate Dynamics*, 17(2–3), 205–212. <https://doi.org/10.1007/s003820000104>
- Piper, D. Z., & Dean, W. E. (2002). *Trace-element deposition in the Cariaco Basin, Venezuela Shelf; under sulphate-reducing conditions: A history of the local hydrography and global climate, 20 ka to the present (1670)*. Reston, VA: U.S. Geological Survey. Retrieved from <http://pubs.er.usgs.gov/publication/pp1670>
- Polissar, P. J., Abbott, M. B., Wolfe, A. P., Vuille, M., & Bezada, M. (2013). Synchronous interhemispheric Holocene climate trends in the tropical Andes. *Proceedings of the National Academy of Sciences of the United States of America*, 110(36), 14551–14556. <https://doi.org/10.1073/pnas.1219681110>
- Portilho-Ramos, R. C., Chiessi, C. M., Zhang, Y., Mulitza, S., Kucera, M., Siccha, M., et al. (2017). Coupling of equatorial Atlantic surface stratification to glacial shifts in the tropical rainbelt. *Scientific Reports*, 7(1), 1561. <https://doi.org/10.1038/s41598-017-01629-z>
- Poveda, G., Waylen, P. R., & Pulwarty, R. S. (2006). Annual and inter-annual variability of the present climate in northern South America and southern Mesoamerica. *Paleogeography, Palaeoclimatology, Palaeoecology*, 234(1), 3–27. <https://doi.org/10.1016/j.palaeo.2005.10.031>
- Prado, L. F., Wainer, I., & Chiessi, C. M. (2013). Mid-Holocene PMIP3/CMIP5 model results: Intercomparison for the South American Monsoon System. *The Holocene*, 23(12), 1915–1920. <https://doi.org/10.1177/0959683613505336>
- Prado, L. F., Wainer, I., Chiessi, C. M., Ledru, M.-P., & Turcq, B. (2013). A mid-Holocene climate reconstruction for eastern South America. *Climate of the Past*, 9(5), 2117–2133. <https://doi.org/10.5194/cp-9-2117-2013>
- Reimer, P. J., Bard, E., Bayliss, A., Beck, J. W., Blackwell, P. G., Ramsey, C. B., et al. (2013). IntCal13 and Marine13 Radiocarbon Age Calibration Curves 0–50,000 Years cal BP. *Radiocarbon*, 55(4), 1869–1887. https://doi.org/10.2458/azu_js_rc.55.16947
- Revel, M., Ducassou, E., Skonieczny, C., Colin, C., Bastian, L., Bosch, D., et al. (2015). 20,000 years of Nile River dynamics and environmental changes in the Nile catchment area as inferred from Nile upper continental slope sediments. *Quaternary Science Reviews*, 130, 200–221. <https://doi.org/10.1016/j.quascirev.2015.10.030>
- Rothwell, R. G., & Croudace, I. W. (2015). Twenty Years of XRF Core Scanning Marine Sediments: What Do Geochemical Proxies Tell Us? In I. W. Croudace, & R. G. Rothwell (Eds.), *Micro-XRF studies of sediment cores: Applications of a non-destructive tool for the environmental sciences* (pp. 25–102). Dordrecht: Springer Netherlands.
- Rühlemann, C., Frank, M., Hale, W., Mangini, A., Mulitza, S., Müller, P. J., & Wefer, G. (1996). Late Quaternary productivity changes in the western equatorial Atlantic: Evidence from 230 Th-normalized carbonate and organic carbon accumulation rates. *Marine Geology*, 135(1), 127–152. [https://doi.org/10.1016/S0025-3227\(96\)00048-5](https://doi.org/10.1016/S0025-3227(96)00048-5)
- Salati, E., Dall'Olio, A., Matsui, E., & Gat, J. R. (1979). Recycling of water in the Amazon Basin: An isotopic study. *Water Resources Research*, 15(5), 1250–1258. <https://doi.org/10.1029/WR015i005p01250>
- Schneider, T., Bischoff, T., & Haug, G. H. (2014). Migrations and dynamics of the intertropical convergence zone. *Nature*, 513(7516), 45–53. <https://doi.org/10.1038/nature13636>
- Shimizu, M. H., Sampaio, G., Venancio, I. M., & Maksic, J. (2020). Seasonal changes of the South American monsoon system during the Mid-Holocene in the CMIP5 simulations. *Climate Dynamics*, 54(5–6), 2697–2712. <https://doi.org/10.1007/s00382-020-05137-1>
- Sifeddine, A., Spadano Albuquerque, A. L., Ledru, M.-P., Turcq, B., Knoppers, B., Martin, L., et al. (2003). A 21 000 cal years paleoclimatic record from Caçó Lake, northern Brazil: evidence from sedimentary and pollen analyses. *Paleogeography, Palaeoclimatology, Palaeoecology*, 189(1), 25–34. [https://doi.org/10.1016/S0031-0182\(02\)00591-6](https://doi.org/10.1016/S0031-0182(02)00591-6)
- Smith, C. B., Cohen, M. C. L., Pessenda, L. C. R., França, M. C., Guimarães, J. T. F., Rossetti, D. d. F., & Lara, R. J. (2011). Holocene coastal vegetation changes at the mouth of the Amazon River. *Review of Palaeobotany and Palynology*, 168(1), 21–30. <https://doi.org/10.1016/j.revpalbo.2011.09.008>
- Snow, J. (1976). The climate of northern South America: Colombia. In W. Schwerdtfeger (Ed.), *Climates of south and Central America* (pp. 358–379). Amsterdam: Elsevier Scientific Publishing Company.
- Strikis, N. M., Cruz, F. W., Cheng, H., Karmann, I., Edwards, R. L., Vuille, M., et al. (2011). Abrupt variations in South American monsoon rainfall during the Holocene based on a speleothem record from central-eastern Brazil. *Geology*, 39(11), 1075–1078. <https://doi.org/10.1130/g32098.1>
- Stuiver, M., & Reimer, P. J. (1993). Extended 14C Data Base and Revised CALIB 3.0 14C Age Calibration Program. *Radiocarbon*, 35(1), 215–230. <https://doi.org/10.1017/s0033822200013904>
- Taylor, K. E., Stouffer, R. J., & Meehl, G. A. (2012). An overview of CMIP5 and the experiment design. *Bulletin of the American Meteorological Society*, 93, 13. <https://doi.org/10.1175/bams-d-11-00094.1>
- Thunell, R. C. (1976). Optimum indices of calcium carbonate dissolution, in deep-sea sediments. *Geology*, 4(9), 525–528. [https://doi.org/10.1130/0091-7613\(1976\)4<525:OIOCCD>2.0.CO;2](https://doi.org/10.1130/0091-7613(1976)4<525:OIOCCD>2.0.CO;2)
- U.S. Environmental Protection Agency. (1996). *Method 3052: Microwave assisted acid digestion of siliceous and organically based matrices*. Test methods for evaluating solid waste, physical/chemical methods (pp. 1–20). Washington D.C.: U.S. Government Publishing Office.
- Utida, G., Cruz, F. W., Etourneau, J., Bouloubassi, I., Schefuß, E., Vuille, M., et al. (2019). Tropical South Atlantic influence on Northeastern Brazil precipitation and ITCZ displacement during the past 2300 years. *Scientific Reports*, 9(1), 1698. <https://doi.org/10.1038/s41598-018-38003-6>
- van Kreveld, S. A., Knappertsbusch, M., Ottens, J., Ganssen, G. M., & van Hinte, J. E. (1996). Biogenic carbonate and ice-rafted debris (Heinrich layer) accumulation in deep-sea sediments from a Northeast Atlantic piston core. *Marine Geology*, 131(1), 21–46. [https://doi.org/10.1016/0025-3227\(95\)00143-3](https://doi.org/10.1016/0025-3227(95)00143-3)

- Vera, C., Baez, J., Douglas, M., Emmanuel, C. B., Marengo, J., Meitin, J., et al. (2006). The South American Low-Level Jet Experiment. *Bulletin of the American Meteorological Society*, 87(1), 63–78. <https://doi.org/10.1175/BAMS-87-1-63>
- Viana, J. C. C., Sifeddine, A., Turcq, B., Albuquerque, A. L. S., Moreira, L. S., Gomes, D. F., & Cordeiro, R. C. (2014). A late Holocene paleoclimate reconstruction from Boqueirão Lake sediments, northeastern Brazil. *Palaeogeography, Palaeoclimatology, Palaeoecology*, 415, 117–126. <https://doi.org/10.1016/j.palaeo.2014.07.010>
- Voigt, I., Cruz, A. P. S., Mulitza, S., Chiessi, C. M., Mackensen, A., Lippold, J., et al. (2017). Variability in mid-depth ventilation of the western Atlantic Ocean during the last deglaciation. *Paleoceanography*, 32, 948. PA003095. <https://doi.org/10.1002/2017PA003095>
- Wang, X., Edwards, R. L., Auler, A. S., Cheng, H., Kong, X., Wang, Y., et al. (2017). Hydroclimate changes across the Amazon lowlands over the past 45,000 years. *Nature*, 541(7636), 204–207. <https://doi.org/10.1038/nature20787>
- Xie, P., & Arkin, P. A. (1997). Global Precipitation: A 17-year monthly analysis based on gauge observations, satellite estimates, and numerical model outputs. *Bulletin of the American Meteorological Society*, 78(11), 2539–2558. [https://doi.org/10.1175/1520-0477\(1997\)078<2539:GPAYMA>2.0.CO;2](https://doi.org/10.1175/1520-0477(1997)078<2539:GPAYMA>2.0.CO;2)
- Xiong, Z., Li, T., Chang, F., Algeo, T. J., Clift, P. D., Bretschneider, L., et al. (2018). Rapid precipitation changes in the tropical West Pacific linked to North Atlantic climate forcing during the last deglaciation. *Quaternary Science Reviews*, 197, 288–306. <https://doi.org/10.1016/j.quascirev.2018.07.040>
- Yancheva, G., Nowaczyk, N. R., Mingram, J., Dulski, P., Schettler, G., Negendank, J. F. W., et al. (2007). Influence of the intertropical convergence zone on the East Asian monsoon. *Nature*, 445(7123), 74–77. <https://doi.org/10.1038/nature05431>
- Zhang, Y., Chiessi, C. M., Mulitza, S., Sawakuchi, A. O., Häggi, C., Zabel, M., et al. (2017). Different precipitation patterns across tropical South America during Heinrich and Dansgaard-Oeschger stadials. *Quaternary Science Reviews*, 177, 1–9. <https://doi.org/10.1016/j.quascirev.2017.10.012>
- Zhang, Y., Chiessi, C. M., Mulitza, S., Zabel, M., Trindade, R. I. F., Hollanda, M. H. B. M., et al. (2015). Origin of increased terrigenous supply to the NE South American continental margin during Heinrich Stadial 1 and the Younger Dryas. *Earth and Planetary Science Letters*, 432, 493–500. <https://doi.org/10.1016/j.epsl.2015.09.054>
- Zhao, Y., Braconnot, P., Marti, O., Harrison, S. P., Hewitt, C., Kitoh, A., et al. (2005). A multi-model analysis of the role of the ocean on the African and Indian monsoon during the mid-Holocene. *Climate Dynamics*, 25(7–8), 777–800. <https://doi.org/10.1007/s00382-005-0075-7>
- Zhou, J., & Lau, K.-M. (1998). Does a Monsoon Climate Exist over South America? *Journal of Climate*, 11(5), 1020–1040. [https://doi.org/10.1175/1520-0442\(1998\)011<1020:DAMCEO>2.0.CO;2](https://doi.org/10.1175/1520-0442(1998)011<1020:DAMCEO>2.0.CO;2)
- Zocatelli, R., Turcq, B., Boussafir, M., Cordeiro, R. C., Disnar, J. R., Costa, R. L., et al. (2012). Late Holocene paleoenvironmental changes in Northeast Brazil recorded by organic matter in lacustrine sediments of Lake Boqueirão. *Palaeogeography, Palaeoclimatology, Palaeoecology*, 363–364, 127–134. <https://doi.org/10.1016/j.palaeo.2012.08.021>
- Zular, A., Utida, G., Cruz, F. W., Sawakuchi, A. O., Wang, H., Bicego, M., et al. (2018). The effects of mid-Holocene fluvio-eolian interplay and coastal dynamics on the formation of dune-dammed lakes in NE Brazil. *Quaternary Science Reviews*, 196, 137–153. <https://doi.org/10.1016/j.quascirev.2018.07.022>